CHAIR OF THERMAL PROCESSING TECHNOLOGY
Head of Department:
Univ.Prof. Dipl.Ing. Dr.techn. Harald Raupenstrauch
University of Leoben
Franz-Josef-Strasse 18
A-8700 Leoben

Master Thesis

Development of a Discrete Particle Model with chemical reactions, mass and heat transfer

created at the

Chair of Thermal Processing Technology

Submitted by:
Zlatko Raonic BSc.
00831838

Supervisors:
Univ.Prof., Dipl.-Ing., Dr.techn. Harald Raupenstrauch
Dipl. Ing., Dr.mont. Christoph Spijker

EIDESSTATTLICHE ERKLÄRUNG

Ich erkläre an Eides statt, dass ich die vorliegende Arbeit selbstständig verfasst, andere als die angegebenen Quellen/Hilfsmittel nicht benutzt, und die den benutzten Quellen wörtlich und inhaltlich entnommenen Stellen als solche kenntlich gemacht habe.

Datum

(Unterschrift)

STATUTORY DECLARATION

I declare that I have authored this thesis independently, that I have not used other than the declared sources / resources, and that I have explicitly marked all material which has been quoted either literally or by content from the used sources.

Date

Signature

Danksagung

Ich möchte mich recht herzlich bei Univ.-Prof. Dipl.-Ing. Dr. techn. Harald Raupenstrauch und Dipl.-Ing. Dr.mont Christoph Spijker für die hervorragende Betreuung bedanken. Ich hatte das Glück, sehr große Unterstützung zu bekommen in fachlicher wie auch in menschlicher Hinsicht.

Abstract

For modelling of numerous heterogeneous dispersion systems under consideration of chemical and physical phenomena, Lagrangian particle tracking model coupled with an Eulerian approach for a continuous fluid phase and additional models for description of mass and heat transport, absorption and chemical reactions, provides the suitable tool . Within scope of this work the state of the art review has been done and possible solutions were examined. Subsequently, the findings and elaborations were applied to two technical questions. The first of these questions, the dispersion of lycopodium particles in test apparatus for dust explosions is approximated using the OpenSource CFD platform OpenFOAM ® with a focus on particle-turbulence interaction. The second application describes the absorption of the easily soluble gaseous ammonia and the sparingly soluble chlorine gas through spray droplet wall with the water as solvent. The commercial CFD software ANSYS-FLUENT® was chosen for this application.

Kurzfassung

Zur Modellierung heterogener dispergierten Systeme unter Betrachtung chemischer und physikalischer Phänomene, stellt Lagrange'sches Partikelmodell gekoppelt mit einer kontinuierlichen Eulerschen Gasphase und Modellen für Stofftransport, Wärmetransport und chemische Reaktionen ein geeignetes Werkzeug dar. Im Rahmen dieser Arbeit wurde der Stand der Technik erhoben und Lösungen für solche Aufgabenstellungen behandelt. Anschließend wurden die Erkenntnisse und Ausarbeitungen auf zwei technische Fragestellungen angewendet.Die erste dieser Fragestellungen, die Verteilung von Lykopodiumpartikel in einer Versuchsapparatur für Staubexplosionen, wurde mit der OpenSource CFD-Plattform OpenFOAM ® gelöst. Der zweite Anwendungsfall beschreibt die Absorption des leicht löslichen gasförmigen Ammoniaks und des schwerlöslichen Chlorgases durch eine Sprühnebel- bzw. Sprühtropfenwand, als Lösungsmittel wurde Wasser verwendet. Für diesen Anwendungsfall wurde die kommerzielle CFD-Software ANSYS-FLUENT® gewählt.

Contents

Chapter 1

Introduction

1.1 Background

Transport of dispersed particles or droplets in a surrounding fluid has a wide range of application in different technical processes such as particle separation, spray drying, spray columns, coal and liquid combustion and some other kind of particle-laden flows. Discrete Particle Model (DPM) as a multiphase approach enables tracking the motion of the large number of individual particles on different time and length scales in a fluid continuum in order to obtain detailed exchange of impulse, mass, energy or any other relevant physical quantity between phases. In the Euler-Euler multiphase approach, the phases are considered as interpenetrating continua, therefore conservation laws are applied to each phase and every individual particle. In Euler-Lagrange (DPM) approach computation of particle trajectories is based on Newton's laws solving only one additional equation of particle motion, making this approach computationally beneficial. Still, it neglects possible boundary layer phenomena such as flow separation and vortex shedding. Basic requirement for the model implementation is the low volume fraction of the dispersed phase, although there is no limitation for the mass loading of secondary phase. The interaction between particles can be considered as well, still the computational time increases dramatically. Influence of the continuous on the dispersed phase manifests basically through drag force and turbulence phenomena, additional acceleration forces such as thermophoretic and virtual mass force are case dependent, while vice versa can be neglected in most of practical cases, it can be included as well.

1.2 Objectives

The aim of this thesis was to develop a general Discrete Particle Model in ANSYS-FLUENT® and OpenFOAM ® that can be extended and adapted to different technically relevant applications. Therefore, the basic model has been implemented for the prediction of time-varying dispersion of Lycopodium particles in a pipe using OpenFOAM ®. A simulation model in ANSYS-FLUENT® was developed to describe dispersion of ammonia and chlorin with additional chemical kinetics to dechlorinate water drops with sodium thiosulfate, and extended for Flash-Reactor pilot plant constructed for recovery of zinc and iron from steel mill dusts. Additionally, analytic solution for velocity profile in droplet formation region of the spray propagation based on the theory of similarity profiles and maximum entropy principle is examined.

Chapter 2

General Model

2.1 Modeling principles

The solution domain is subdivided into finite number of discrete control volumes and for each of them a set of differential equations is solved numerically. Finite Volume Method is suitable for complex grids, using surface and volume integrals that are conservative by its form for mathematical approximation of physical phenomena, which combined with strong conservation form of Navier-Stokes equations insures global momentum conservation in the calculation domain.

2.1.1 Euler-Lagrange

The numerical calculation of two-phase flows with a low volume fraction of dispersed phase is based on a coupled hybrid approach.

Observation of a physical quantities for the fixed volume cell over the time step is called Eulerian-approach. Fluid flow is calculated on continuum assumption solving Navier-Stokes equation for a fixed volume element, modeling time dependent change in the control volume and flux of physical quantities over the volume surface.

Lagrangian approach follows dispersed particles in the space over the time, describing particle path line through the continuous phase. Lagrangian method is used for tracking of a large number of particles considering momentum, energy and species exchange with the continuous phase within each cell on the particle path.[Ferziger and Perić, 2002]

The difference between Eulerian and Lagrangian approach is demonstrated in Figure 2.1.

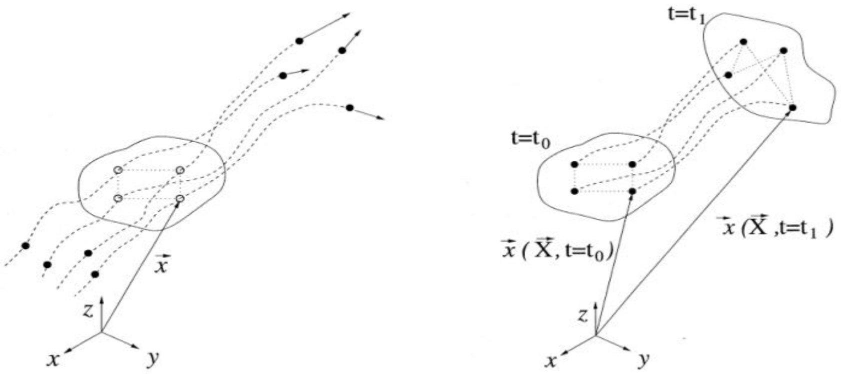

(a) Eulerian approach (b) Lagrangian approach

Figure 2.1: Euler-Lagrange [Brenn and Steiner, 2005]

2.2 Governing equations

2.2.1 Continuous Phase

Continuous Phase section is mainly based on [Ferziger and Perić, 2002] and [Ansys Inc, 2013], unless explicitly stated otherwise for additional literature.

Relation between temperature, velocity, pressure and density in a fluid flow is described by the set of coupled Navier-Stokes equations. Integral form of the mass conservation equation can be written as:

$$\frac{\partial}{\partial t}\int\limits_{\Omega}\rho d\Omega + \int\limits_{\mathbb{S}}\rho\mathbf{v}\cdot\mathbf{n}d\mathbb{S} = 0 \tag{2.1}$$

Transforming surface flux of a vector field in the convection therm into the volume integral of the divergence for the same field over the volume region defined by the closed surface, a differential form of the continuity equation is obtained :

$$\frac{\partial\rho}{\partial t} + \nabla(\rho\cdot\mathbf{v}) = 0 \tag{2.2}$$

Similarly, the momentum conservation equation for a fixed volume describes balance between temporal momentum change and its divergence in control volume and corresponding forces that act on the fluid in a control volume:

$$\frac{\partial}{\partial t}\int\limits_{\Omega}\rho\mathbf{v}d\Omega + \int\limits_{\mathbb{S}}\rho\mathbf{v}\mathbf{v}\cdot\mathbf{n}d\mathbb{S} = \sum\mathbf{f} \tag{2.3}$$

The term on the right hand side of the equation represents surface forces such as pressure, normal and shear stress, surface tension etc., and body forces, e.g. gravity, electromagnetic, centrifugal forces, etc. Taking stresses and body force per unit mass into consideration Equation 2.3 becomes :

$$\frac{\partial}{\partial t}\int\limits_{\Omega}\rho\mathbf{v}d\Omega + \int\limits_{\mathbb{S}}\rho\mathbf{v}\mathbf{v}\cdot\mathbf{n}d\mathbb{S} = \int\limits_{\mathbb{S}}\mathbf{T}\cdot\mathbf{n}d\mathbb{S} + \int\limits_{\Omega}\rho\mathbf{b}d\Omega \tag{2.4}$$

The stress Tensor for Newtonian fluids can be written symbolically as:

$$\mathbf{T} = -\Big(p + \frac{2}{3}\mu\nabla\cdot\mathbf{v}\Big)\mathbb{I} + 2\mu\mathbf{D} \tag{2.5}$$

with rate of strain:

$$\mathbf{D} = \frac{1}{2}[\nabla\mathbf{v} + (\nabla\mathbf{v})^T]. \tag{2.6}$$

In index notation in Cartesian coordinates:

$$\mathbf{T_{ij}} = -\Big(p + \frac{2}{3}\mu\frac{\partial u_j}{\partial x_j}\Big)\delta_{ij} + 2\mu\mathbf{D_{ij}} \tag{2.7}$$

$$\mathbf{D_{ij}} = \frac{1}{2}\Big(\frac{\partial u_i}{\partial x_j} + \frac{\partial u_j}{\partial x_i}\Big) \tag{2.8}$$

with Kronecker delta:

$$\delta_{ij} = \begin{cases} 1, & \text{if } i = j \\ 0, & \text{otherwise} \end{cases}$$

Viscous part of the stress tensor can be written in the form:

$$\tau_{\mathbf{ij}} = -\frac{2}{3}\mu\delta_{ij}(\nabla\cdot\mathbf{v}) + 2\mu\mathbf{D_{ij}} \tag{2.9}$$

Applying Gauss' divergence theorem in Equation 2.4 and considering identical calculation domain:

$$\frac{\partial(\rho\mathbf{v})}{\partial t} + \nabla\cdot(\rho\mathbf{v}\mathbf{v}) = \nabla\cdot\mathbf{T} + \rho\mathbf{b} \tag{2.10}$$

Above equation in conservative form for the ith component in Cartesian coordinates becomes:

$$\frac{\partial(\rho u_i)}{\partial t} + \nabla\cdot(\rho u_i\mathbf{v}) = \nabla\cdot\mathbf{t_i} + \rho\mathbf{b_i} \tag{2.11}$$

Insertion of continuity Equation 2.2 in Equation 2.11 leads to non-conservative form of impulse equation[1] :

$$\rho\frac{\partial u_i}{\partial t} + \rho\mathbf{v}\cdot\nabla u_i = \nabla\cdot\mathbf{t_i} + \rho\mathbf{b_i} \tag{2.12}$$

Substituting Equation 2.9 for viscous part in Equation 2.11 considering gravity and additional force $\mathbb{F}$ caused by interaction with dispersed phase written in Cartesian coordinates, we obtain:

$$\frac{\partial(\rho u_i)}{\partial t} + \frac{\partial(\rho u_i u_j)}{\partial x_j} = \frac{\partial\tau_{ij}}{\partial x_j} - \frac{\partial p}{\partial x_i} + \rho g_i + \mathbb{F}_i \tag{2.13}$$

Analogously, conservation of any scalar quantity ϕ in integral form can be defined as follows:

$$\frac{\partial}{\partial t}\int_{\Omega}\rho\phi d\Omega + \int_{\mathbb{S}}\rho\phi\mathbf{v}\cdot\mathbf{n}d\mathbb{S} = \sum\mathbf{f}_{\phi}, \tag{2.14}$$

where f_ϕ quantifies transport of ϕ. Thus, the energy equation can be written as :

$$\frac{\partial}{\partial t}\int_{\Omega}\Big[\rho\Big(e+\frac{\mathbf{v^2}}{2}\Big)\Big]d\Omega + \int_{\mathbb{S}}\Big[\rho\Big(e+\frac{\mathbf{v^2}}{2}\Big)\Big]\mathbf{v}\cdot\mathbf{n}d\mathbb{S} = \int_{\Omega}(\rho\mathbf{v}\cdot\mathbf{b})d\Omega - \int_{\mathbb{S}}p\mathbf{v}\cdot\mathbf{n}d\mathbb{S} + \int_{\mathbb{S}}(\mathbf{v}\cdot\mathbf{T}^*)\mathbf{n}d\mathbb{S} + \int_{\mathbb{S}}\mathbf{q}\cdot\mathbf{n}d\mathbb{S} + \int_{\Omega}\dot{\mathbf{q}}d\Omega, \tag{2.15}$$

---

[1] $\nabla\cdot(\rho\mathbf{v}u_i) = u_i\nabla\cdot(\rho\mathbf{v}) + \rho\mathbf{v}\cdot\nabla u_i$

with

$$\mathbf{T}^* = \mathbf{T} + p\mathbb{I}$$

as viscous part of the stress tensor.

Equation 2.15 can be written symbolically as:

$$\frac{\partial}{\partial t}\Big[\rho\Big(e + \frac{\mathbf{v^2}}{2}\Big)\Big] + \Big[\nabla \cdot \rho\mathbf{v}\Big(e + \frac{\mathbf{v^2}}{2}\Big)\Big] = \rho\mathbf{v} \cdot \mathbf{b} - \nabla \cdot p\mathbf{v} + \nabla \cdot (\mathbf{T}^* \cdot \mathbf{v}) - \nabla \cdot \mathbf{q} + \dot{\mathbf{q}} \tag{2.16}$$

The first four therms on the right hand-side of the Equation 2.16 represent work done by body force, pressure work, viscous dissipation and energy transfer due to conduction, respectively. The last therm stands for any relevant volumetric heat source, such as heat of chemical reaction or radiation.

2.2.1.1 Reynolds-Averaged Navier-Stokes (RANS) Equations

The transition between laminar and turbulent flow depends on ratio of inertial to viscous forces, called Reynolds number. In laminar case, fluid flows in layers so that fluid particle follows the streamlines exactly, with convective impulse and heat transport occurring only in the mean flow direction.

Turbulent flows are unsteady, characterized by stochastic three-dimensional changes of velocity and vortices of different size interacting with each other. Fluid parcels with differing concentrations of the conserved properties are increasingly brought into contact enhancing mixing rate. This process is also called turbulent diffusion, effect that can increase chemical mixing and heat transfer by orders of magnitude. Additionally, due to viscosity, reduction of the velocity gradient causes irreversible kinetic energy decrease which is converted into internal energy of fluid. Although there is coherent structure in turbulent flow regimes, as some aspects on the larger scale appear to be quasi-deterministic, the randomness still occurs as difference in geometric shape, temporal behavior and intensity, making it difficult to define the model that represents all kind of turbulent flows.

Time averaging approach in Reynolds-Averaged Navier-Stokes(RANS) enables modeling of the unsteadiness as the part of turbulence considering it engineering approximation. The field properties in turbulent flows are random functions of space and time but any variable can be expressed as the sum of mean and fluctuating part:

$$\phi(x,t) = \overline{\phi}(x_i) + \phi'(x_i,t), \tag{2.17}$$

where

$$\overline{\phi}(x_i) = \lim_{T\to\infty} \frac{1}{T} \int_0^T \phi(x_i,t), \tag{2.18}$$

for a statistically steady flow.

Averaging interval T must be large enough compared to fluctuations time scale so that $\bar{\phi}$ is independent from the given starting point for averaging. For unsteady flow, ensemble averaging is used instead of time averaging:

$$\overline{\phi}(x_i) = \lim_{T\to\infty} \frac{1}{T} \sum_{n=1}^{N} \phi(x_i,t) \tag{2.19}$$

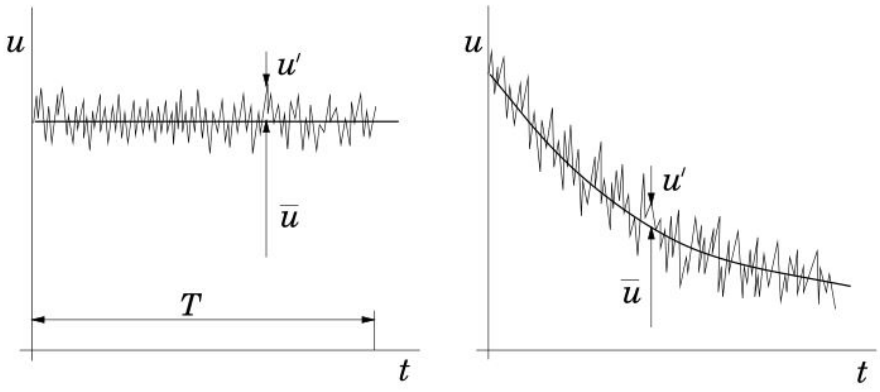

Figure 2.2: Time averaging for steady (left) and unsteady (right) turbulent flow [Ferziger and Perić, 2002]

Average of linear therm is identical therm, whereas averaging of quadratic non-linear therm yields the product of the average and a covariance:

$$\overline{u_i\phi} = \overline{(\overline{u}_i + u_i')(\overline{\phi} + \phi')}. \tag{2.20}$$

Described ensemble and time averaging concept for steady and unsteady turbulent flow conditions is illustrated in Figure 2.2.
Hence, substituting velocity u_i and pressure p expressed as a sum of mean and fluctuating part into Equation 2.13, considering Equation 2.20 yields to Reynolds averaged Navier Stokes:

$$\frac{\partial(\rho\overline{u}_i)}{\partial t} + \frac{\partial}{\partial x_j}(\rho\overline{u}_i\overline{u}_j + \rho\overline{u_i'u_j'}) = -\frac{\partial\overline{p}}{\partial x_i} + \frac{\partial\overline{\tau}_{ij}}{\partial x_j} + \rho g_i + \mathbb{F}_i, \tag{2.21}$$

with time averaged continuity :

$$\frac{\partial\rho}{\partial t} + \frac{\partial(\rho\overline{u}_i)}{\partial x_i} = 0 \tag{2.22}$$

Finally we can derive the equation for the mean of the scalar quantity:

$$\frac{\partial\rho\overline{\phi}}{\partial t} + \frac{\partial}{\partial x_j}(\rho\overline{u}_j\overline{\phi} + \rho\overline{u_j'\phi'}) = \frac{\partial}{\partial x_j}\left(\Gamma\frac{\partial\overline{\phi}}{\partial x_j}\right) \tag{2.23}$$

Decomposition of the instantaneous values into mean and fluctuating part introduced new unknown quantities with no additional equations making the system underdetermined. Closure requires modeling approximations of the therms such as $\rho\overline{u_i'u_j'}$, called Reynolds stresses, and turbulence scalar flux $\rho\overline{u_j'\phi'}$, in form of turbulence models, as it is impossible to define a closed set of analytic equations.

2.2.1.2 Turbulence Modeling

Turbulence models are based on empirical experience and experimental data, and there is no model that is universally accepted. Therefore, important decision criteria are flow characteristics and computational costs combined with capabilities and limitations of various models, such as convergence behavior and accuracy degree.

Reynolds Stress Model

Reynolds Stress Model (RSM) is one of the most sophisticated model in common use that closes Reynolds-Averaged Navier-Stokes as the Reynolds stresses are determined by solution of transport equations and turbulence energy dissipation rate ϵ. It is computational more expensive compared to other common used models, with potential for superior predictive accuracy due to conservative formulation. Important characteristic of the model is prediction of anisotropy in the Reynolds stresses, which is especially relevant in highly swirling turbulent flows. Still, for pressure strain therm, dissipation and turbulent diffusion tensor, approximate modeling is necessary for closure. Although, some good results have been obtained compared to two equation models, especially in the cases where $k - \epsilon$ models perform poorly, in some cases it's numerical accuracy is hardly better. The research in this field develop continuously and better models are often proposed.
[Launder et al., 1975]

Eddy-viscosity model

Eddy-viscosity model for the Reynolds stress is based on assumption that turbulence can be described as an increased viscosity effect:

$$\rho\overline{u_i'u_j'} = \mu_t\Big(\frac{\partial\overline{u}_i}{\partial x_j} + \frac{\partial\overline{u}_j}{\partial x_i}\Big) - \frac{2}{3}\rho\delta_{ij}k, \tag{2.24}$$

with turbulent kinetic energy k defined as:

$$k = \frac{1}{2}\overline{u_i'u_i'} = \frac{1}{2}(\overline{u_x'u_x'} + \overline{u_y'u_y'} + \overline{u_z'u_z'}). \tag{2.25}$$

Eddy-diffusion model for a scalar is given by :

$$-\rho\overline{u_j'\phi'} = \Gamma_t\frac{\partial\overline{\phi}}{\partial x_j}. \tag{2.26}$$

There are two additional equations necessary to describe k and μ_t quantities.

k-epsilon model

K-epsilon ($k - \epsilon$) turbulence model is the most widely used model providing excellent results for some kind of flows at relatively low computational costs. There are numerous exemplary studies and comparative calculations verifying implementability for turbulent flows with high Reynolds number exclusive swirling flows, flows with stagnation points and strong geometry curvatures.
The equation that describes transport of turbulent kinetic energy k is as follows:

$$\frac{\partial(\rho k)}{\partial t} + \frac{\partial(\rho\overline{u}_j k)}{\partial x_j} = \frac{\partial}{\partial x_j}\Big[\Big(\mu + \frac{\mu_t}{\sigma_k}\Big)\frac{\partial k}{\partial x_j}\Big] + \mu_t\Big(\frac{\partial\overline{u}_i}{\partial x_j} + \frac{\partial\overline{u}_j}{\partial x_i}\Big)\frac{\partial\overline{u}_i}{\partial x_j} - \rho\epsilon \tag{2.27}$$

Derivation of exact equation for the transport formulation of turbulent kinetic energy is described in [Wilcox, 2010], which mainly used as information source in this section. The term of the right-hand side of

Equation 2.27 multiplied by $\frac{\mu_t}{\sigma_k}$ represents turbulent diffusion of kinetic energy that approximates transport of velocity fluctuations by the fluctuations themselves.
The second term on the right-hand side of the Equation 2.27 represents the rate of production of turbulent kinetic energy, i.e. transfer of turbulent kinetic energy from the mean flow. Turbulent Prandtl number σ_k has approximately value of unity.
The last term represents the rate at which the turbulence energy is irreversibly converted into internal energy. All the other terms can be calculated directly.

The most commonly used form of equation for the dissipation of turbulent kinetic energy ϵ can be written as:

$$\frac{\partial(\rho\epsilon)}{\partial t} + \frac{\partial(\rho\bar{u}_j\epsilon)}{\partial x_j} = \mathbb{C}_{\epsilon 1}\mathbb{P}_k\frac{\epsilon}{k} - \rho\mathbb{C}_{\epsilon 2}\frac{\epsilon^2}{k} + \frac{\partial}{\partial x_j}\Big(\frac{\mu_t}{\sigma_k}\frac{\partial\epsilon}{\partial x_j}\Big), \tag{2.28}$$

with turbulent viscosity expressed by k and ϵ as follows:

$$\mu_t = \rho\mathbb{C}_\mu\frac{k^2}{\epsilon}, \tag{2.29}$$

and $\mathbb{P}_k$ describes the rate of production of the turbulent kinetic energy. Two new partial differential equations that are much stiffer than the laminar equations need to be solved. The constants are determined from simplified flow conditions that are experimentally validated for fully developed turbulent flows.
The most commonly used values for model constants that are empirically determined based on labor experiments are given in Table 2.2:

$\mathbb{C}_\mu$	$\mathbb{C}_{\epsilon 1}$	$\mathbb{C}_{\epsilon 1}$	σ_k	σ_ϵ
0.09	1.44	1.92	1.0	1.3

Table 2.1: $k-\epsilon$ model constants

relizable k-epsilon model

Modification of standard k-epsilon has improved predictions of the model, especially for jet streams This model, compared to standard $k-\epsilon$, has the same formulation for transport of turbulent kinetic energy equation, but improved equation for dissipation rate equation . Furthermore, it is known that standard $k-\epsilon$ model becomes non-realizable in the case of large mean strain rate, so that model constant C_μ must be set variable and related to mean strain. Modified model shows improved predictions for flows involving planar and round jets (predicts round jet spreading correctly), boundary layers under strong adverse pressure gradients or separation, rotation, recirculation and strong streamline curvature.[Shih et al., 1995]

k-omega model

In this model equation for the transport of turbulent kinetic energy (Equation 2.27) is modified to:

$$\frac{\partial(\rho k)}{\partial t} + \frac{\partial(\rho \overline{u}_j k)}{\partial x_j} = \mu_t \Big(\frac{\partial \overline{u}_i}{\partial x_j} + \frac{\partial \overline{u}_j}{\partial x_i} \Big) \frac{\partial \overline{u}_i}{\partial x_j} - \beta^* \rho k \omega + \frac{\partial}{\partial x_j} \Big[\Big(\mu + \sigma^* \frac{k}{\omega} \Big) \frac{\partial k}{\partial x_j} \Big]. \tag{2.30}$$

Transport equation for ω represents the specific dissipation rate of energy, often described as frequency characteristic of the turbulence decay process:

$$\frac{\partial(\rho \omega)}{\partial t} + \frac{\partial(\rho \overline{u}_j \omega)}{\partial x_j} = \alpha \frac{\omega}{k} \mu_t \Big(\frac{\partial \overline{u}_i}{\partial x_j} + \frac{\partial \overline{u}_j}{\partial x_i} \Big) \frac{\partial \overline{u}_i}{\partial x_j} - \beta \rho \omega^2 + \frac{\partial}{\partial x_j} \Big[\Big(\mu + \sigma \frac{k}{\omega} \Big) \frac{\partial \omega}{\partial x_j} \Big] + \frac{\sigma_d}{\omega} \frac{\partial k}{\partial x_j} \frac{\partial \omega}{\partial x_j}. \tag{2.31}$$

Eddy viscosity in this model is calculated as:

$$\mu_t = \rho \frac{k}{\omega}. \tag{2.32}$$

First therm on the right-hand side in Equation 2.30 and Equation 2.31 represents transfer from the mean flow to the turbulence, the second therm stands for turbulent diffusion, third therm represents an irreversible conversion of the quantity, respectively. Left-hand side of both equations has a form of total differential for given quantity. Additionally, the last therm in Equation 2.31 proportional to σ_k, known as cross-diffusion, has been introduced to eliminate boundary condition sensitivity. Still, model made in this manner is limited in applicability to wall-bounded flows.

α	β	β^*	σ_k	σ_ϵ
$\frac{13}{25}$	0.072	0.09	2	2

Table 2.2: $k - omega$ model constants

Standard $k-\omega$ shows good prediction accuracy for laminar-turbulent transition zone and it is model of choice for the treatment of sublayer region with sufficient accuracy in logarithmic region with a good prediction of the mean flow. It has an advantage compared to $k-\epsilon$ for the geometries with strong curvatures due to better stability characteristic. Although the production terms added to $k - \omega$ model improved prediction accuracy for free shear flows, sensitivity of the solutions to values for k and ω outside the shear layer still remains, even when very small boundary conditions for turbulence parameter(e.g., k and ν_t) are chosen.
Because of this freestream sensitivity model can not be used for free jet calculation with satisfactory results. [Wilcox, 2010]

Shear-Stress Transport k-omega

Shear-Stress Transport (SST) $k - \omega$ is combination of existing models that uses original $k - \omega$ in the inner region of the boundary layer taking advantage of $k - \epsilon$ in outer region and free shear flow. The blending function switches between one in the sublayer and logarithmic region of the boundary activating standard

$k-\omega$ and gradually switches to zero for the flow regions away from the wall boundary activating $k-\epsilon$ model. The difference between SST and the original model is additional cross-diffusion term in the equation with newly formulated modeling constants and modified definition of eddy viscosity.
For further information can be found in the refer [Menter, 1994].

Near Wall Treatment

The profile of turbulence is significantly influenced in the near wall region due to no slip condition on the wall that reduces tangential velocity fluctuations and absence of kinetic energy fluctuation in normal direction. However, in the outer part of the near wall region, production of turbulent kinetic energy is enhanced by large mean velocity gradients. Although, the turbulent production cycle in the inner region appears to be self-sustaining, the outer structure has at least a Reynolds number dependent influence on the near-wall phenomena.
The experiments have shown that turbulent boundary layer can be divided into three characteristic layers. In the inner region of the viscous sublayer with almost laminar flow where the viscosity is dominant for momentum, heat and mass transfer. Between outer fully turbulent layer and viscous sublayer there is an intermediate region with viscous and turbulent effects of equal importance.

There are two possible approaches for modeling turbulence effects near the wall:

- viscous sublayer and buffer layer in the inner region is treated with semi-empirical formulas called wall functions
- turbulence models are implemented in the viscosity-affected region that is resolved with enough grid points. The quality of obtained results depends on sufficient mesh refinement in boundary layer needed to cover it accurately.

At high Renolds number very thin viscous sublayer makes it difficult to use enough grid points to resolve it. In that case, the wall functions that rely on existence of a logarithmic region are used, as shown in Figure 2.3.

The velocity profile in the logarithmic layer is given by:

$$u^+ = \frac{\overline{v}_t}{u_\tau} = \frac{1}{\kappa} ln(y^+) + B. \tag{2.33}$$

Here κ is the von Karman constant, B is an empirical constant related to the thickness of viscous sublayer, v_t is the mean velocity parallel to the wall with u_τ as the shear velocity defined by:

$$u_\tau = \sqrt{\frac{|\tau_w|}{\rho}}, \tag{2.34}$$

and n_+ is dimensionless distance to the wall given as:

$$y^+ = \frac{\rho u_\tau y}{\mu} \tag{2.35}$$

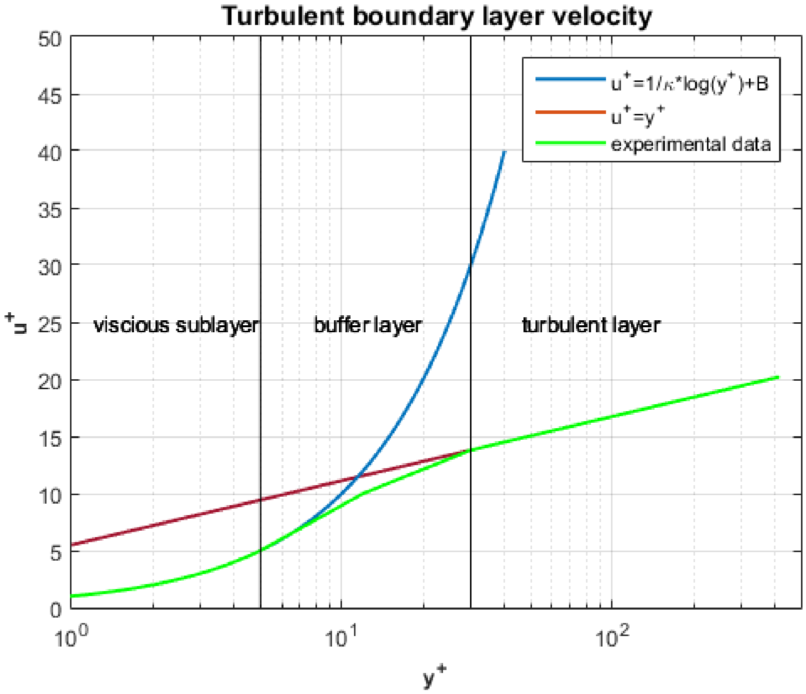

Figure 2.3: Velocity profile as a function of distance normal to wall in the turbulent boundary layer

Under assumption that the production and dissipation of turbulence are in local equilibrium shear velocity can be written in the form:

$$u_\tau = C_\mu^{\frac{1}{4}}\sqrt{k} \tag{2.36}$$

Reynolds analogy between physical mechanism of heat and momentum transfer enables similar description of the turbulent boundary layer for the temperature:

- linear law for the thermal conduction sublayer
- logarithmic law for the turbulent region where effects of turbulence dominate conduction

Further information can be found in the literature cited. [Wilcox, 2010],[Stephen Kern Robertson, 1991]

2.2.1.3 Radiation Model

Dependent on their temperature all materials emit or absorb thermal radiative energy in the form of electromagnetic waves which require no medium for propagation. While there is more or less linear dependency on temperature difference of conductive and convective heat transfer, radiative heat flux is proportional to fourth power of temperature differences between sources. Therefore, radiation is the dominant mode of heat transfer in high-temperature processes, as well as in low pressure (vacuum) applications .
In most engineering applications where radiative thermal energy is of relevance, participating medium is not transparent but possibly emitting, absorbing or eventually scattering radiation.

Radiative Transfer Equation (RTE)

To describe the propagation of thermal radiation between bounding walls within participating medium that absorbs, scatters and transmits electromagnetic waves, it is necessary to solve the RTE:

$$\frac{d\mathbb{I}_\lambda}{ds} = \hat{s}\cdot\nabla\mathbb{I}_\lambda = \kappa_\lambda \mathbb{I}_{b\lambda} - \beta_\lambda \mathbb{I}_\lambda + \frac{\sigma_{s\lambda}}{4\pi}\int\limits_{4\pi} \mathbb{I}_\lambda(\hat{s}_i)\Phi_\lambda(\hat{s}_i,\hat{s})d\Omega_i. \tag{2.37}$$

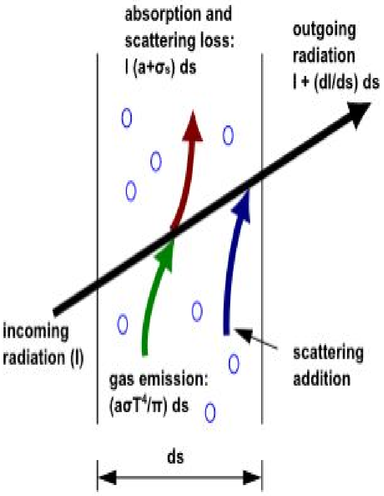

Figure 2.4: Radiative heat transfer [Ansys Inc, 2013]

Integration of the RTE over all spatial directions and wave-lengths leads to the radiative heat flux. In the Equation 2.37 κ_λ stands for the medium's absorption coefficient, $\sigma_{\lambda s}$ represents its scattering coefficient,$\beta_\lambda = \kappa_\lambda + \sigma_{\lambda s}$ is so called extinction coefficient, and Φ_λ is the scattering phase function.

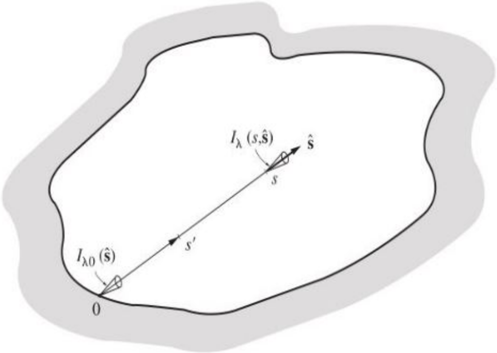

Figure 2.5: Coordinates definition for the radiative heat transfer equation [Bejan and Kraus, 2003]

As illustrated in Figure 2.5, Equation 2.37 specifies spectral radiative intensity $\mathbb{I}_\lambda$ along a path s in the direction of $\hat{s}$, quantifying the increment by emission along the path, attenuation by extinction, absorption and outscattering of radiation away from $\hat{s}$ and increase by in-scattering from all other directions $\hat{s}_i$. Where, κ_λ quantifies relatively how much radiation is absorbed or emitted, $\sigma_{\lambda s}$ gives a relative measure of how much is scattered, and Φ_λ is the probability function for radiation scattered from $\hat{s}_i$ into $\hat{s}$ direction.[Bejan and Kraus, 2003]

Discrete Transfer Radiation Model (DTRM) Theory

Neglecting radiative scattering in medium with assumption for refractive index to be unity Equation 2.37 can be integrated from boundary wall along the ray path:

$$\mathbb{I}_\lambda(s) = \mathbb{I}_\lambda(0)e^{-\kappa_\lambda s} + \int\limits_0^s \mathbb{I}_{b\lambda}(s')e^{-\kappa_\lambda(s-s')}\kappa_\lambda ds' \tag{2.38}$$

If absorption coefficient is assumed constant and medium is considered isothermal to the point $s' = s$:

$$\mathbb{I}_\lambda(s) = \mathbb{I}_\lambda(0)e^{-\kappa_\lambda s} + \mathbb{I}_{b\lambda}(1 - e^{-\kappa_\lambda s}) \tag{2.39}$$

With the following relation for spectral emissivity, transmissivity and absorptivity:

$$\epsilon_\lambda(s) = \alpha_\lambda(s) = 1 - \tau_\lambda(s) = 1 - e^{-\kappa_\lambda s}, \tag{2.40}$$

Equation 2.39 can be written as:

$$\mathbb{I}_\lambda(s) = \mathbb{I}_\lambda(0)\tau_\lambda(s) + \mathbb{I}_{b\lambda}\epsilon_\lambda(s) \tag{2.41}$$

Taking StefanBoltzmann law into consideration with $\mathbb{I}(0)$ defined as radiative intensity on the boundary, the above expression becomes:

$$\mathbb{I}(s) = \frac{\sigma T^4}{\pi}(1 - e^{-\kappa s}) + \mathbb{I}(0)e^{-\kappa s}, \tag{2.42}$$

where
T...gas local temperature in K
σ... Stefan-Boltzmann constant $5.670373 \cdot 10^{-8} \frac{W}{m^2 K^4}$.

For numerical solution in DTRM discrete angles of the polar and azimuthal angles are calculated dependent on number of pre-defined rays from each radiating face and subsequently the ray paths through discretized control volume are determined. Polar and azimuthal angles $0 < \Theta < \frac{\pi}{2}$ and $0 < \Phi < 2\pi$ at the point P are defined over tangential and normal vector throw the point on the surface, as shown in Figure 2.6

The advantage of DTRM race tracing method is that radiation between surfaces is estimated without necessity to explicitly calculate view factors which is computationally more expensive.

Higher number of ray traces and the finer the mesh grid, the more accurate is DTRM calculation.

Main disadvantage of the model is that it considers only gray radiation with isotropic reflection at the surface. [Bejan and Kraus, 2003]

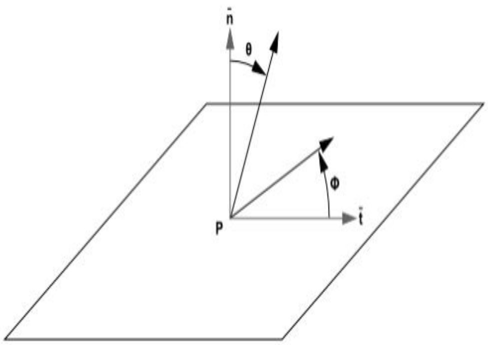

Figure 2.6: DTRM polar and azimuthal angles [Ansys Inc, 2013]

Discrete Ordinates (DO) Radiation Model

DO radiation model solves Equation 2.37 considering absorption, emission, and scattering in medium enabling dependency of the radiation variables from the wave length and other physical quantities such as local temperature, pressure and species concentration.

The method uses exactly the same discretized finit-volume mesh as the fluid equations, satisfying global conservation balance. Transport equation for radiation is solved in spatial coordinates for every direction $\hat{s}$ for a chosen number of discrete solid angles defined as shown in Figure 2.7:

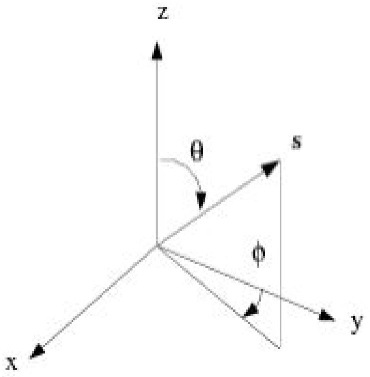

Figure 2.7: DO angular coordinate system [Ansys Inc, 2013]

The model enables implementation of the non-gray radiation through the definition of variable spectral absorption over the different bands. In the same manner, assuming that the emission and absorption are constant within each band, it is possible to model gas behavior at diverse wave numbers. It is possible to define spectral emissivity at the radiating wall, as well. DO method has improved convergence behavior for problem set-ups with optical thick-nesses greater than 10 which is typical for glass-melting applications. Still, model has some limitations that must be considered:

- for the case with weak directional intensity radiation and energy coupling, model has quite slow convergence behavior
- DO model cannot be coupled with energy equation for the case that enthalpy equation is solved instead of temperature.

[Raithby and Chui, 1990]

2.2.2 Discrete Phase

2.2.2.1 Drop formation

Description of drop formation phenomena in this section is mainly based on following literature : [Bailey et al., 1983],[Chad et al., 2009].
For the mass transfer and chemical reactions with dispersed droplets and its interaction with the continuous phase, drop formation process is of essential importance. Drop size distribution depends on fluid viscosity, surface tension coefficient, nozzle geometry and nozzle surface roughness, liquid velocity and the environment that surrounds nozzle.
Influence of the interaction with the surrounding medium depends on existent fluid movement (relative velocity) and therefore arising aerodynamic forces that breaks up the stream of fluid working against physical properties of surface tension, viscosity, and density.
As those properties are temperature dependent, it affects the process of atomization as well.

The spray nozzle geometry design affects drop size of the spray with the largest drop size produced by full cone nozzle, smaller by hollow cone nozzle and the very fine drops are provided by air assisted nozzles. It should be noted that nozzle wear influences uniformity of the spray pattern.

Fluid impulse caused by the pressure in the nozzle influences droplet size - higher pressure means higher velocity which decreases average droplet size and vice versa.

Ratio between fluid inertial force and surface tension that is useful for description of atomization phenomena is dimensionless number called Weber number :

$$We = \frac{\rho u^2 l}{\sigma}, \tag{2.43}$$

with ρ, u, σ representing fluid density the droplet is dispersed in, velocity and surface tension coefficient respectively and l stands for characteristic length. An other representation form is modified Weber We^* defined as ratio of the kinetic energy of on impact to surface energy:

$$We^* = \frac{We}{12} = \frac{E_k}{E_s}, \tag{2.44}$$

with kinetic energy given by:

$$E_k = \frac{\pi \rho l^3 u^2}{12} \tag{2.45}$$

and surface energy:

$$E_s = \pi l^2 \sigma \tag{2.46}$$

In general, surface tension is the influential property that prevents break up, whereas higher velocity increases friction between fluid and surrounding medium leading to a droplet formation at some critical value.

Similar effect to surface tension has fluid viscosity, as the quantity for the fluid resistance to deformation.

It means that the smaller values of surface tension and viscosity and higher fluid pressure that causes higher velocity once the fluid leaves the nozzle, with other properties remaining constant, lead to a formation of smaller droplets.

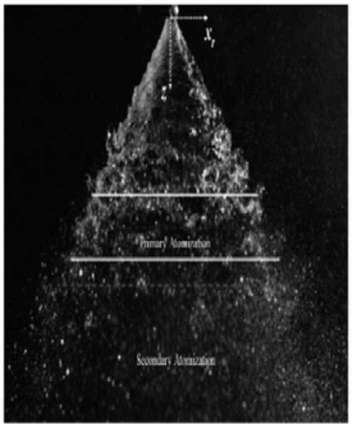

Figure 2.8: Atomisation Process [Chad et al., 2009]

In the airless atomization process, due to high pressure the fluid is forced throw the nozzle orifice emerging as a solid stream or sheet at a high speed, dependent on Weber number value. The friction between the fluid and the surrounding gas breaks the stream into fragments and then into droplets. The droplet formation is not only characterized by the drop size in primary atomization but as well by the extend at which the large droplets are breaking up further in the secondary atomization area. These distinctive areas are shown in Figure 2.8.

For the spray distributions, it is common to rely on statistical descriptive measures to characterize the size distribution.

The simplest integral characterization is mean diameter given by:

$$d_{30} = \frac{\sum d_i n_i}{\sum n_i} \tag{2.47}$$

where D_i is the diameter of the i-th class and n_i is the frequency.

Considering mass and heat transfer, an important parameter is the total surface of the dispersed phase, i.e. ratio of volume to surface. Droplet diameter with a same ratio of volume to surface as a considered spray that is appropriate for the representative prediction of system behavior is called Sauter mean diameter:

$$d_{32} = \frac{\sum d_i^3 n_i}{\sum d_i^2 n_i} \tag{2.48}$$

As it can be seen from last two equations, droplet spectrum change has less significant influence on the mean diameter. Many empirical probability density functions have been developed for description of droplet size distribution in sprays that can be used for extraction of spray mean diameters out of available data. The most well known are Nukiyama-Tanasawa, Rosin-Rammler and upper limit distribution. Rosin-Rammler is common mathematical representation for the drop size distribution which is used in this work as well. Limitations in the use of this distribution for liquid droplet ensembles to fit existing experimental data are discussed in [Bailey et al., 1983].

Formula proposed by Rosin and Rammler is as follows:

$$R(d) = 100e^{\left(\frac{d}{d'}\right)^n} \tag{2.49}$$

In the equation above $R(d)$ is the cumulative volume fraction in percent of droplet material greater than d, $d^{'}$ is size parameter and n is distribution spread parameter. A double logarithm of the Equation 2.49 under consideration that n and $d^{'}$ are the constants calculated from the data set yields:

$$log\Big(log\frac{100}{R(d)}\Big) = n \cdot logd - n \cdot logd^{'} + log(loge) \tag{2.50}$$

Distribution spread parameter n is given by following equation:

$$n = \frac{log\Big(log\frac{100}{R(d_2)}\Big) - log\Big(log\frac{100}{R(d_1)}\Big)}{logd_2 - logd_1}, \tag{2.51}$$

where $[d_1, R(d_1)]$ and $[d_2, R(d_2)]$ are random collinear data points.

Size parameter $d^{'}$ is calculated from Equation 2.49 inserting $d = d^{'}$, which is diameter level of approximately 36,78 cumulative percent of material. Rosin-Rammler distribution with double logarithm of $100/R(d)$ on y axis over logarithm of d on x for operating point 9 from Table 4.1 with $n = 1.8821$ and $d^{'} = 753\mu m$ is shown in Figure 2.9.

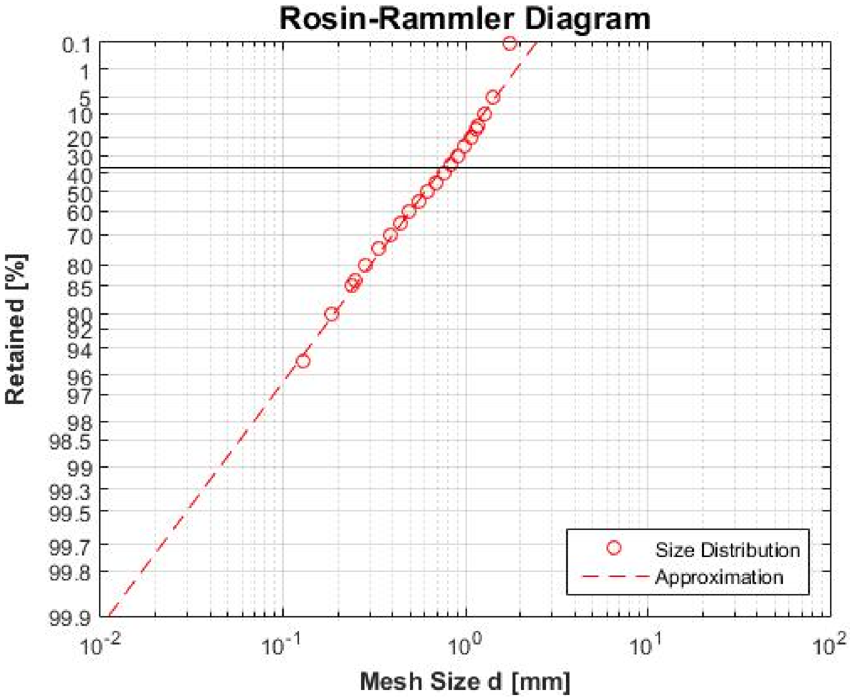

Figure 2.9: Rosin Rammler distribution

2.2.2.2 Droplet size distribution

Droplet size distribution is the initial condition for the numerical simulation that can be determined either experimentally or modeled mathematically based on maximum entropy principle.

The principle used for the optical droplet size measurement is based on Frauenhofer diffraction of monochromatic light on moving particles, where diffraction pattern is related to the droplet size. Intensity of scattered light is measured using photo diodes and additionally converted into droplet diameters. The limitation of this technique is multiple scattering problem in the dense regions of the spray as the light beam can be scattered by multiple drops. Multiple scattering phenomena leads to broader distribution spectrum and smaller droplet average size.[Lefebvre and McDonell, 2017]

2.2.2.3 Jet characteristics and droplet velocity

Jet characterization and velocity profile definition described in this section is based on [Ball et al., 2012],[Cha et al., 2017],[Hussein et al., 1994].
Figure Figure 2.10 illustrates formation of a round jet from the nozzle exit in the surrounding ambient. Potential core occurs in the region of flow establishment, starting at the exit of the contraction nozzle. Jet instability on the interface between surrounding medium and outer border of the jet propagation, leads to a formation of vortices in the mixing zone. Vortices development, intensity and further coupling in the flow

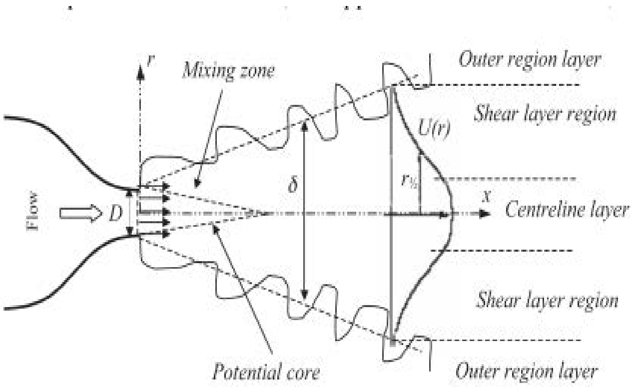

Figure 2.10: Free jet formation [Ball et al., 2012]

field depends entirely on the initial conditions, which have decisive influence on the flow development in the entire flow domain as well.

In the radial direction, there are three distinctive layers as shown in Figure 2.10: centerline region, the shear layer and outer region with following with following specific physical properties:

- maximum mean velocity in the jet flow is located in the centerline region.
- vortices caused by radial velocity gradients evolve in the shear layer region and create so called large eddies.
- large scale turbulent motions in shear layer diminish in time and space, creating smaller structures through energy transfer with the velocity in outer layer of $U_C/10$ order.

Entrainment of surrounding air increases mass flow along the axial direction in the free jet, where as momentum conservation is satisfied.

Conventionally, axial spreading of a axisymmetric turbulent round free jet in the air surrounding, which is of the relevance in this work, is divided into three characteristic regions.

The mean velocity profile at nozzle outlet is determined by the type, i.e. geometry. From the nozzle outlet the near field region with a potential core is located in a range within approximately $0 \leq x/D \leq 7$, where D is a nozzle diameter, with a negligible air carryover. Within this region of the flow establishment the turbulence is generated in the mixing zone between jet and surrounding. The mean velocity profile is strongly dependent on the nozzle geometry.

Transition zone expands over the range of $7 \leq x/D \leq 70$. In this region comes to additional interaction between dispersed and continuous phase with an air carryover effect and phase mixing with the reduction of average velocity. This region is characterized with highly anisotropic turbulent structures.

The far field region expands in a range of $x/D \leq 70$. In this region of so called self-similar velocity profiles occurs an intensive impulse transmission form the droplets to surrounding medium with the slip-free streaming assumption. The flow is considered to be in equilibrium, which according to Kolmogorov's Universal

Equilibrium Theory means that ”small scale eddies are locally isotropic and in approximate statistical equilibrium with the large scale eddies”.

Thin shear layer approximation is here valid, i.e. radial gradients are for many orders of magnitude larger than axial gradients. Conservation of momentum is satisfied in the flow field, as it must be, but mass flow changes with the entrainment of the surrounding air.

As the flow development depends directly on density ratio between jet fluid and surrounding medium, it is of importance in a case of two phase jet flow to use effective radius as physically meaningful and more appropriate characteristic length, given by:

$$r_{\epsilon} = r_{nozzle}\frac{\rho_e}{\rho_{\infty}}, \tag{2.52}$$

where ρ_e is the density of medium on nozzle exit and ρ_{∞} is density of ambient.

With isothermal conditions or negligibly small temperature differences between nozzle outlet and surrounding atmosphere, for the determination of the velocity profile is only impulse of the streaming medium from the relevance.

Furthermore, a homogeneous stationary velocity is assumed through the nozzle outlet with an idealized rotationally symmetrical profile of the free stream with a zero velocity on the outside margin.

For the fully developed far field region the centreline mean velocity U_C decay is linear dependent on axial distance from the nozzle exit:

$$\frac{U_e}{U_c} = V_{DR}\Big(\frac{X - X_{U1}}{D_{\epsilon}}\Big), \tag{2.53}$$

where U_e stands for the mean velocity on the nozzle exit, X for axial distance from the nozzle exit, X_{U1} is the kinematic virtual origin, i.e. the axial end point position of the potential core length and V_{DR} is the velocity decay rate. Figure Figure 2.11 illustrates velocity decay on the centerline of the free jet in the far field region for $70 \leq X/D \leq 150$, for all operating points given in Table 4.1.

The values for model constants used in Equation 2.53 for V_{DR} and X_{U1} are 6.06 and 7, respectively. Decay rate of centerline velocity regarding to jet velocity on nozzle outlet for the operating points is illustrated in Figure 2.12.

The characteristic radius $r_{V,0.5}$ where the local mean velocity U_m in radial direction has a value $U_C/2$ is used for the quantification of jet spreading:

$$\frac{r_{V,0.5}}{D} = V_{SR}\Big(\frac{X - X_{U2}}{D}\Big), \tag{2.54}$$

where X_{U2} is geometrical virtual origin. The maximum spreading radius defining border line on the measurement plane without dispersed particles for given axial distance of the measurement point has been determined experimentally.

As reported by several authors, geometrical and kinematic virtual origins are not necessary identical but still of much smaller order than the geometrical scale of fully developed velocity profiles.

In this work, it is assumed that high velocity on nozzle outlet with small nozzle diameter causes almost immediate drop formation process so that kinematic virtual origin is negligibly small compared to relevant

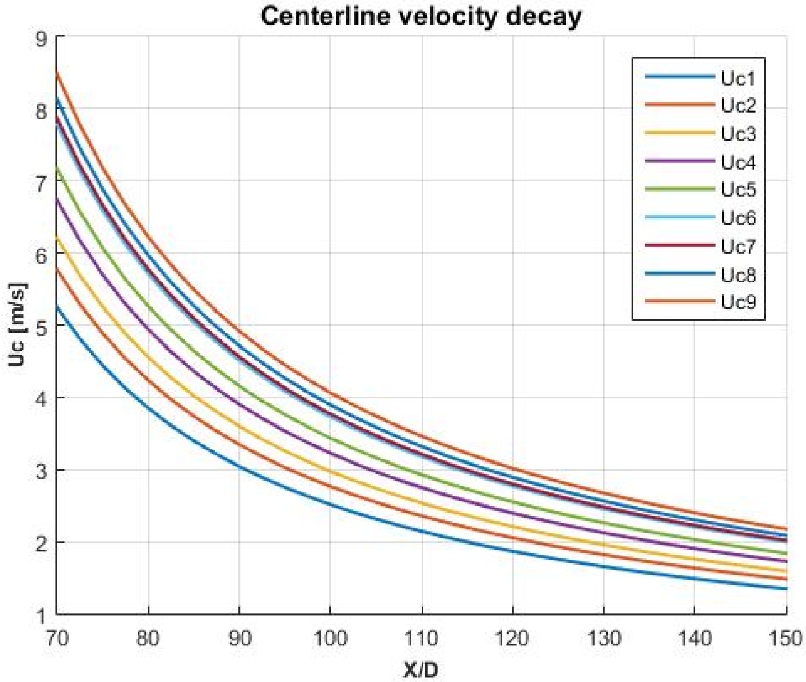

Figure 2.11: Centerline velocity decay

axial distance and therefore not considered.

Based on initial Gaussian distribution following equation was used for calculation of velocity profiles dependent on axial distance from nozzle outlet and half-width radius:

$$\frac{U(X,r)}{U_c(X)} = e^{\left\{-ln2(\frac{r}{r_{V,0.5}})^2\right\}} \tag{2.55}$$

Velocity profiles normal to the measurement plane for X/D in the jet spreading direction dependent on vertical distance to centerline plotted against radius normalized by nozzle diameter are shown in figure Figure 2.13. Those are used as initial condition for the free jet simulation. Velocity profiles $U(r)$ normilezed by centerline velocity at measurement point $X/D = 85$ are shown in Figure 2.14

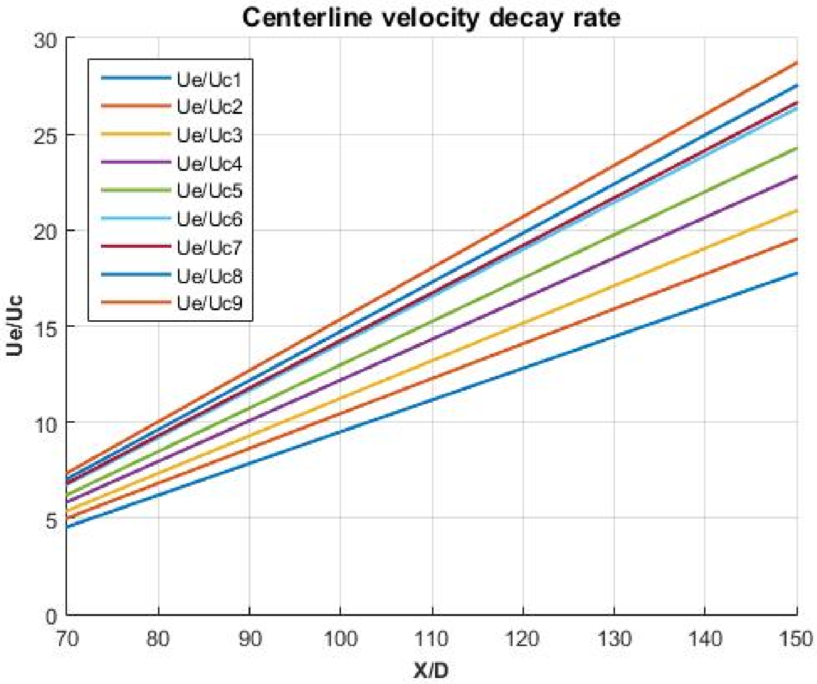

Figure 2.12: Centerline velocity decay

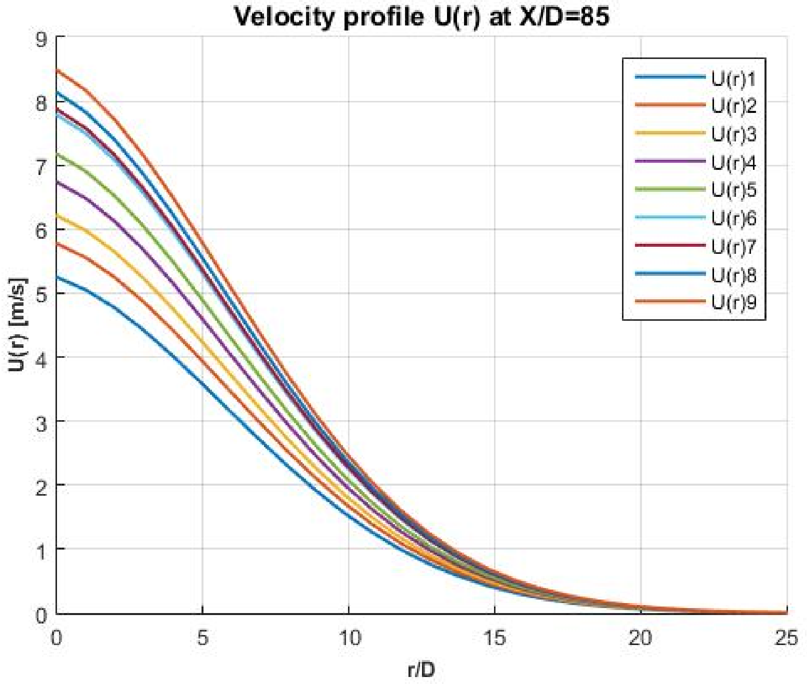

Figure 2.13: Velocity profiles U(r)at measurement point

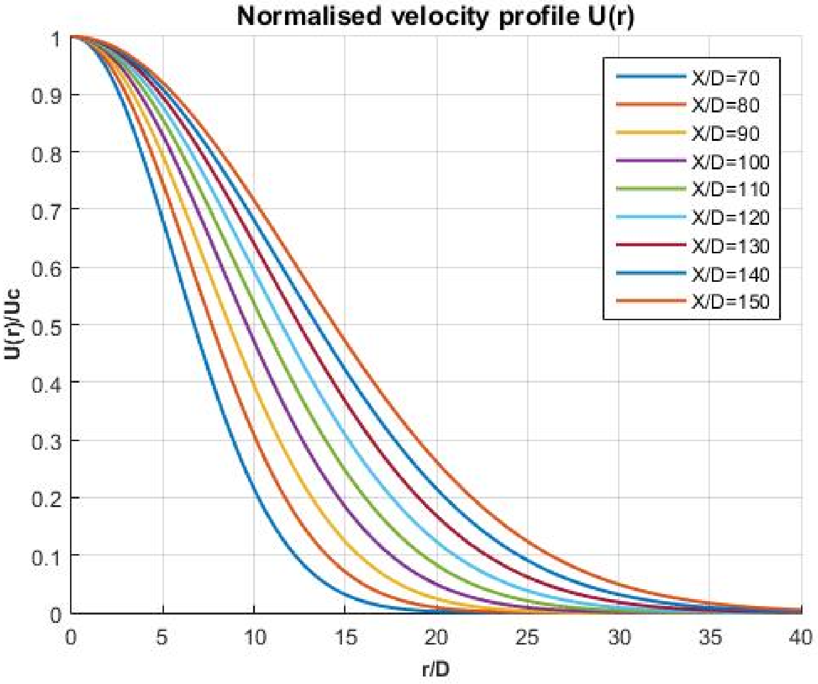

Figure 2.14: Velocity profile U(r) normilezed by center line velocity

2.2.2.4 Maximum entropy principle

This section is based on following literature: [Dumouchel, 2009],[Movahednejad et al., 2010],[Movahednejad et al., 2011],[Kim et al., 2003],[Mohammad-Djafari, 2002].

As the liquid flows downstream from the nozzle exit decrease of the liquid sheet thickness leads to instabilities, i.e. fragmentation in ligaments and finally to drop formation. From the mathematical point of view atomisation process of a water jet can be divided into two distinctive consecutive phases:

- deterministic process in the beginning stage with characteristic wave motion on the surface of liquid sheet and
- random and stochastic droplet formation.

Deterministic primary phase of spray formation is described with linear and non-linear hydrodynamic instability theories. Dominant wavelength of unstable wave motion on the liquid surface over the time (temporal instability wave growth) and with axial distance from the nozzle (spatial instability wave growth) on the liquid surface, can be determined by linear instability theory. Non-linear instability provides crucial information about break up length and characteristics of the liquid sheets.

Depending on the type of nozzle and other relevant conditions using instability theory (i.e. Weber number based on sheet velocity, two-phase density ratio) a prior droplet size distribution can be formulated to connect deterministic and stochastic part of atomisation process.

Still, with high liquid velocity and small nozzle diameters droplet formation process starts just at the nozzle exit so that liquid sheet and ligaments doesn't occur. In this case it is only random stochastic description that is of the relevance. Implemented predictive droplet size distribution model in this work formulated according to maximum entropy principle is within the framework of these criteria.

Maximum entropy principle is based on information theory and basic physical laws of mass, momentum and total energy (sum of kinetic and surface energy) conservation for the conditions at the nozzle exit. Model formulation enables implementation of any additional source term of the physical influence between exit nozzle and droplet formation plane.

The random stochastic model is defined by formal mathematical formulation of maximum entropy principle based on Claude Shannons entropy formulation:

$$S = -k \sum_{i=1}^{n} p_i ln(p_i), \tag{2.56}$$

where p_i is the probability for the state i to occur and k is Boltzmann constant. Constraints defined by physical quantities that are already known for physical system can be mathematically characterized as follows:

$$\sum_{i=1}^{n} p_i g_{r,i} = \langle g_r \rangle \quad r = 1, 2, ..., m. \tag{2.57}$$

In the equation above n stands for the number of possible possible states of the system, m considers number of defined physical constraints for the particular system, $g_{r,i}$ expresses value of a function for the state i and

$\langle g_r \rangle$ is average value of the function for the entire system.
And finally the constraint that is immanent to the definition of probability:

$$\sum_{i=1}^{n} p_i = 1 \tag{2.58}$$

For the case that number of possible states is equal to number of physical constraints, the number of unknowns becomes equal to number of equations, so that probability distribution can be directly calculated.
For the most of practical problems this is not the case - number of constraints is significantly smaller then the number of possible states. However, making use of the fact that between continuous liquid bulk and completed spray atomisation entropy rises until it reaches maximum, maximizing Equation 2.56 probability distribution p_i can be determined.
Solution for the system of equations that consist of physical constraints that are satisfying conversion laws maximizing entropy function can be found using the method of Lagrange multipliers. It means, we try to find maximum of $S = f(p1, p2, ..., p_n)$ under constraints given by Equation 2.58 and Equation 2.57. The Lagrangian with multiple constraints for this case takes the form:

$$\mathcal{L}(p1, ..., p_n, \lambda_1, ..., \lambda_r) = f(p1, ..., p_n) - \sum_{r=1}^{m} \lambda_r g_r(p1, ..., p_n). \tag{2.59}$$

Thus, following relation has to be solved:

$$\nabla_{p_1,...,p_n,\lambda_1,...,\lambda_m} \mathcal{L}(p_1, ..., p_n, \lambda_1, ..., \lambda_m) = 0 \tag{2.60}$$

$$\Leftrightarrow \nabla f(p) - \sum_{r=1}^{m} \lambda_r \nabla g_r(p) = 0 \tag{2.61}$$

Multiplying Equation 2.58 and Equation 2.57 with λ_0 and and λ_r respectively, taking Equation 2.56 into account and implementing summation of those consecutively in Equation 2.59 and Equation 2.60 following relation is obtained:

$$\sum_{i=1}^{n} \Big[ln(p_i) + \lambda_0 + \sum_{r=1}^{m} \lambda_r g_{r,i} \Big] dp_i = 0 \tag{2.62}$$

Above equation is satisfied if the term in the square bracket equals zero, which leads to:

$$p_i = \sum_{i=1}^{n} exp\Big[-\lambda_0 - \sum_{r=1}^{m} \lambda_r g_{r,i} \Big] \tag{2.63}$$

Maximum entropy principle formulated on this way is applicable only for one dimensional system. For multidimensional system with velocity and droplet size distribution, probability p_i needs to be expanded to joint probability p_{ij}, where indices i, j are denoting correspondent probability states of particle size and velocity that are independent in the domain. Control volume is enclosed by bulk liquid state at the nozzle exit and the plane where the droplets formation occurs. As stated before, for the case that droplet formation starts immediately on the nozzle exit, all additional source terms are vanishing.

Under steady state condition, mass conservation law implies that total mass of droplets per time unit has to be equal to total liquid mass sprayed into surrounding per unit time. Any non-conservative phenomena causing mass transfer between liquid and gaseous phase, such as condensation or vaporization, are considered in an additional source term with corresponding algebraic sign.

For liquid mass flow $\dot{m}_l$ with $\dot{n}$ number of droplets produced per time unit, mass conservation can be written as:

$$\sum_i \sum_j p_{ij} V_i \rho_l \dot{n} = \dot{m}_l + S_m \tag{2.64}$$

The non-dimensional form of the equation is created using velocity at the nozzle exit U_e and mean droplet volume V_m as a reference level:

$$V_m = \frac{\dot{m}_l}{\rho_l \dot{n}} \tag{2.65}$$

$$\overline{V}_i = \frac{V_i}{V_m} \quad \overline{U}_j = \frac{U_j}{U_e} \tag{2.66}$$

With dimensionless mass source term $\overline{S}_m = S_m/\dot{m}_l$ Equation 2.64 takes the following form:

$$\sum_i \sum_j p_{ij} \overline{V}_i = 1 + \overline{S}_m \tag{2.67}$$

Analogously, the dimensionless formulation of impulse and total energy constraints can be written as:

$$\sum_i \sum_j p_{ij} \overline{V}_i \overline{U}_j = 1 + \overline{S}_{vm} \tag{2.68}$$

$$\sum_i \sum_j p_{ij} (\overline{V}_i \overline{U}_j^2 + B' K_i + \overline{V}_i) = 1 + \overline{S}_e, \tag{2.69}$$

where $K_i = A_i/V_i$ denotes the ratio of surface to volume of the droplet from the class i and B' is given by:

$$B' = \frac{2\sigma}{\rho_l U_e^2} \tag{2.70}$$

Continuous droplet size and velocity variation reflects the physical reality more appropriately, therefore summation can be replaced by integral form. Furthermore, we assume that small droplets in the spray have spherical form, which allows mean volume V_m definition in terms of mass mean diameter:

$$V_m = \frac{\pi}{6} D_{30}^3, \tag{2.71}$$

with non-dimensional form:

$$\overline{V} = (\frac{D}{D_{30}})^3 = \overline{D}^3. \tag{2.72}$$

Accordingly infinitesimal dimensionless volume element is expressed by:

$$d\overline{V} = 3\overline{D}^2 d\overline{D}. \tag{2.73}$$

Thus, continuous joint probability density function f for the droplet size and velocity with Lagrange multipliers $\lambda_i (i = 0, 1, 2, 3)$ is defined as follows:

$$\begin{aligned}
&p\{\overline{V}_{n-1} \leqslant \overline{V} \leqslant \overline{V}_n, \overline{U}_{m-1} \leqslant \overline{U} \leqslant \overline{U}_m\} \\
&= p\{\overline{D}_{n-1} \leqslant \overline{D} \leqslant \overline{D}_n, \overline{U}_{m-1} \leqslant \overline{U} \leqslant \overline{U}_m\} \\
&= \int\limits_{\overline{D}_{n-1}}^{\overline{D}_n} \int\limits_{\overline{U}_{m-1}}^{\overline{U}_m} 3\overline{D}^2 exp\{-\lambda_0 - \lambda_1 \overline{D}^3 - \lambda_2 \overline{D}^3 \overline{U} - \lambda_3 (\overline{D}^3 \overline{U}^2 + B\overline{D}^2)\} d\overline{D} d\overline{U} \\
&= \int\limits_{\overline{D}_{n-1}}^{\overline{D}_n} \int\limits_{\overline{U}_{m-1}}^{\overline{U}_m} f d\overline{D} d\overline{U},
\end{aligned} \tag{2.74}$$

where B denotes gas-liquid surface tension coefficient:

$$B = \frac{We}{12}, \tag{2.75}$$

and

$$We = \frac{\rho_l U_e^2 D_{30}}{\sigma}. \tag{2.76}$$

Here, the Weber number is defined differently than usual because of the liquid density ρ_l used for the calculation instead of density of surrounding medium in conventional definition.

Considering probability density function for continuous variables with corresponding minimum and maximum values, the physical constraints for mass, impulse and energy conservation defined in Equation 2.67, Equation 2.68 and Equation 2.69 can be rewritten in integral form:

$$\int\limits_{\overline{D}_{min}}^{\overline{D}_{max}} \int\limits_{\overline{U}_{min}}^{\overline{U}_{max}} f \overline{D}^3 d\overline{D} d\overline{U} = 1 + \overline{S}_m. \tag{2.77}$$

$$\int\limits_{\overline{D}_{min}}^{\overline{D}_{max}} \int\limits_{\overline{U}_{min}}^{\overline{U}_{max}} f \overline{D}^3 \overline{U} d\overline{D} d\overline{U} = 1 + \overline{S}_{vm}. \tag{2.78}$$

$$\int\limits_{\overline{D}_{min}}^{\overline{D}_{max}} \int\limits_{\overline{U}_{min}}^{\overline{U}_{max}} f \frac{1}{H} (\overline{D}^3 \overline{U}^2 + B\overline{D}^2) d\overline{D} d\overline{U} = 1 + \overline{S}_e. \tag{2.79}$$

here H is introduced as additional explanatory variable for the shape factor determined by the outlet velocity profile. For uniform profile it equals to one.

And additionally integral normalization:

$$\int\limits_{\overline{D}_{min}}^{\overline{D}_{max}} \int\limits_{\overline{U}_{min}}^{\overline{U}_{max}} f d\overline{D} d\overline{U} = 1, \tag{2.80}$$

Described method of the maximum entropy formalism is used for numerical calculation of Langrange multipliers. The number based droplet size distribution can be calculated integrating Equation 2.74 from minimum to maximum velocity value in the field:

$$\frac{dN}{d\overline{D}} = \int\limits_{\overline{U}_{min}}^{\overline{U}_{max}} f d\overline{U} \tag{2.81}$$

The minimum velocity value can be set to zero, whereas maximum value depends on secondary break up that occurs at critical Weber number value:

$$We_c = \frac{\rho_g U^2 D}{\sigma} \approx 10 \tag{2.82}$$

Dimensionless maximum droplet velocity can be estimated from the following equation, under assumption that velocity ratio between surrounding air and liquid is negligibly small (otherwise relative velocity has to be considered):

$$\overline{U}_{max} = \Big(\frac{10}{\rho\sigma\overline{D}}\Big)^{1/2} \tag{2.83}$$

Maximum droplet diameter is given by the estimated velocity, whereas the minimum chosen droplet diameter value can be set near zero. It should be noted that extremely high $\overline{U}_{max}$ values are characteristic for very small droplet diameters (submicron range) that are not of physical relevance for practical applications. Analogously to Equation 2.81, number based droplet velocity distribution can be calculated within estimated droplet range:

$$\frac{dN}{d\overline{U}} = \int\limits_{\overline{D}_{min}}^{\overline{D}_{max}} f d\overline{D} \tag{2.84}$$

Comparison between theoretical and experimental droplet size distribution for operating point 9 from Table 4.1 ($p = 11.9bar, V = 0.97l/s, D_{nozzle} = 4mm$) is shown in figure Figure 2.15.

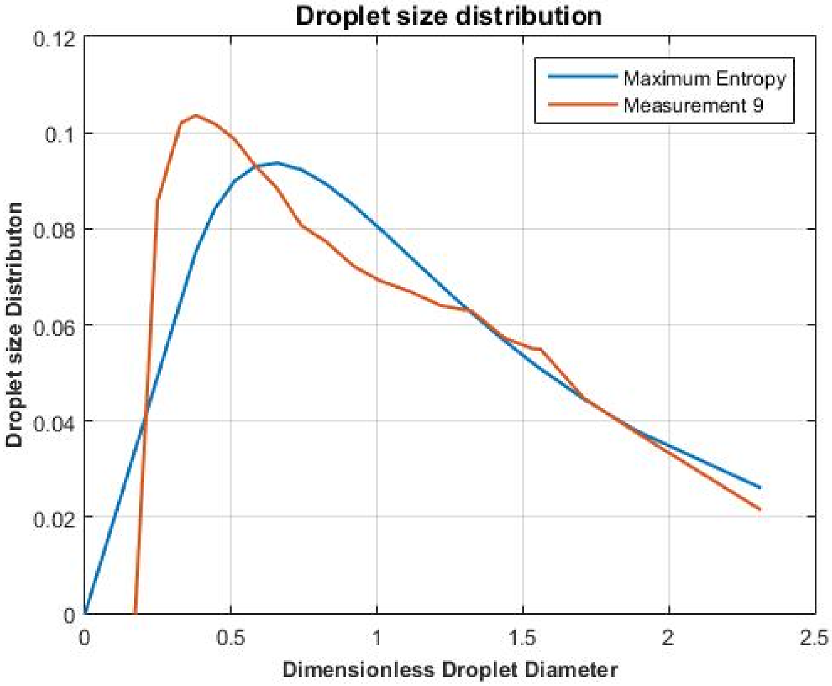

Figure 2.15: Theoretical and experimental droplet size distribution

2.2.2.5 Equation of motion for particle

The equation of motion in a Lagrangian reference frame for a dispersed particle is a balance equation between particle inertia and the forces acting on the particle integrated over time. The equation is given as:

$$\frac{d\vec{u}_p}{dt} = \mathbb{F}_D(\vec{u} - \vec{u_p}) + \frac{\vec{g}(\rho_p - \rho)}{\rho_p} + \vec{\mathbb{F}} \tag{2.85}$$

$\vec{\mathbb{F}}$....additional acceleration force/unit particle mass
$\mathbb{F}_D(\vec{u} - \vec{u_p})$....drag force per unit particle mass, with:

$$\mathbb{F}_D = \frac{18\mu}{\rho_p d_p^2} \frac{\mathbb{C}_d Re}{24} \tag{2.86}$$

Drag coefficient $\mathbb{C}_d$ is defined in Equation 2.93 whereas relative Reynolds number Re is calculated from Equation 2.92. The last therm on the right-hand side includes all additional forces acting on the particle, dependent on the physical conditions.

Particle velocity at each point of the trajectory can be computed from the Equation 2.85, with the differential equation for the particle trajectory given by:

$$\frac{dx}{dt} = u_p \tag{2.87}$$

Solution of coupled ordinary differential equations (Equation 2.85 and Equation 2.87) describes the motion of the particles in the continuous phase.

This approach neglects all the states that may be produced in the immediate vicinity of a particle due to boundary layer phenomena such as flow separation and vortex shedding. [**?**]

Additional virtual mass force

Relative acceleration of the dispersed particle to continuous phase exerts and additional virtual mass force due to inertial fluid mass force caused by acceleration of surrounding fluid.
Virtual mass force can be approximated by following expression:

$$\vec{\mathbb{F}} = \mathbb{C}_{vm}\frac{\rho}{\rho_p}\left(\vec{u_p}\nabla\vec{u} - \frac{d\vec{u_p}}{dt}\right). \tag{2.88}$$

$\mathbb{C}_{vm}$.... empirical constant with default value of 0.5
The pressure gradient in surrounding medium generates and additional force acting on the particle which is given by expression:

$$\mathbb{F} = \frac{\rho}{\rho_p}\vec{u_p}\nabla\vec{u}. \tag{2.89}$$

Equation 2.88 and Equation 2.89 are negligible for the values of $\frac{\rho}{\rho_p} << 1$. [Roco, 1993]

Thermophoretic force

Thermophoretic force is exerted on the particle dispersed in the fluid with the presence of temperature gradient, which is given as:

$$\vec{\mathbb{F}} = -\mathbb{D}_T\frac{1}{m_pT}\nabla T \tag{2.90}$$

From the equation above it is obvious that thermophoretic force is acting in opposite direction to the temperature gradient. The phenomenon is of practical importance by industrial applications with small particles, such as soot, aerosols and similar.
In the literature, several expressions have been proposed for the thermophoretic force on the particle. In this formulation thermophoretic coefficient $\mathbb{D}_T$ can be used as fitting parameter, either as constant or eventually as some special defined function. [Talbot et al., 1980],[Ansys Inc, 2013]

2.2.2.6 Drag coefficient

Crucial factor that influence motion of particle, or the cloud of particles of a low concentration, introduced in an fluid stream, is a drag force determined by relative velocity, i.e by Reynolds number. This assumption is valid if there is no particle interaction and further more no change in the air flow pattern of continuous phase. In general, drops can be approximated as spheres if surface tension and viscous forces are of more importance than inertia forces. In this work small droplets ($d < 2mm$) are considered as spheres, therefore is retroactive effect of droplet deformation on flow around the droplet negligibly small. Otherwise, an alternative multi-phase approach with enhancement to interface reconstruction would be necessary for detailed simulation of the particle deformation effect.

For the laminar flow with very small Reynolds numbers, known as Stokes flow, non dimensional drug coefficient for spherical particle is calculated using the following formula :

$$C_d = \frac{Re_p}{24} \tag{2.91}$$

With relative Reynolds number Re_p defined as:

$$Re = \frac{\varrho d_p |\mathbf{u_p} - \mathbf{u}|}{\mu} \tag{2.92}$$

Beyond the Stokes range, drag coefficient varies with the particle Reynolds number, as shown in Figure 2.16.

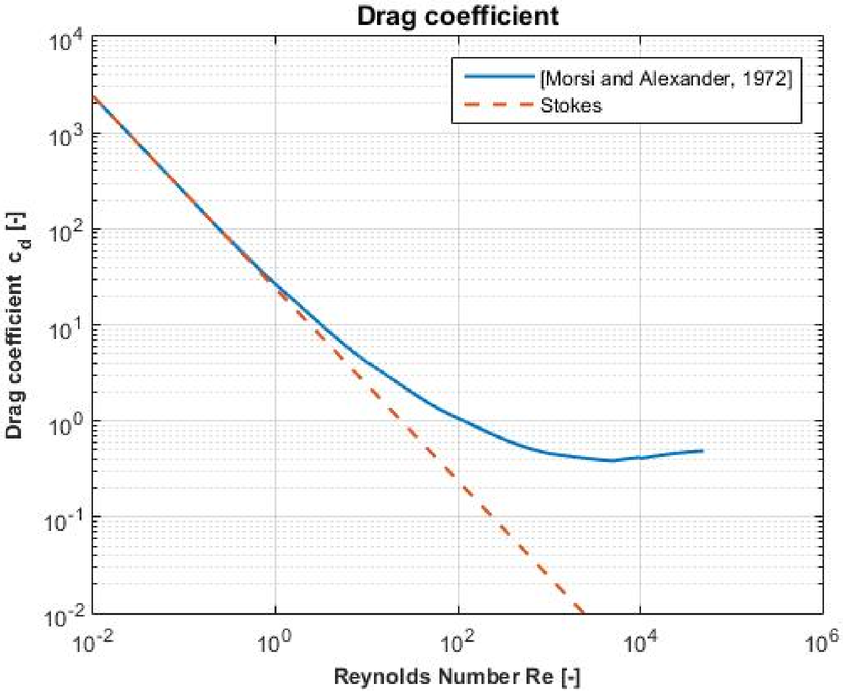

Figure 2.16: Drag Coefficient for spherical particle

Alexander and Morsi suggested empirical formula with coefficient values divided into several sections dependent on Reynolds number, with calculated value within 1-2% of experimentally measured value:

$$C_d = \frac{K_1}{Re_p} + \frac{K_2}{Re_p^2} + K_3. \tag{2.93}$$

Figure 2.16 illustrates drag coefficients as a function of particle Reynolds number for the calculated constants given in Table 2.3.[Morsi and Alexander, 1972]

Particle Reynolds number Re_p	$\mathbb{K}_1$	$\mathbb{K}_2$	$\mathbb{K}_3$
$0 < Re_p < 0.1$	24	0	0
$0.1 < Re_p < 1$	22.73	0.0903	3.69
$1 < Re_p < 10$	29.1667	3.8889	1.222
$10 < Re_p < 100$	46.5	116.67	0.6167
$100 < Re_p < 1000$	98.33	2778	0.3644
$1000 < Re_p < 5000$	148.62	47500	0.357
$5000 < Re_p < 10000$	- 490.546	578700	0.46
$10000 < Re_p < 50000$	- 1662.5	5.4167	0.5191

Table 2.3: Morsi-Alexander Drag Coefficients

2.2.2.7 Particle Collision and Coalescence

Collision and coalescence are important phenomena especially in the regions of high droplet or particle density, whereas coalescence is per definition not possible in the case of solid particles. The number of possible collisions for n particles with n-1 possible collision partners, considering that reverse order of collision partner is same as original one, is $\frac{1}{2}n^2$. In some engineering problems, such as spray propagation, particle number can achieve value of several millions. As the collision model has to calculate all possible particle collisions at every time step it makes calculation costs enormous.

Therefore, definition of a parcel as group of particles which is actually statistical representation of physical particle, reduces computational time significantly.

Furthermore, for enough small continuous phase cell, it can be assumed that two particles can collide only if they are located in the same cell of the continuous phase. After the collision has been determined, collisional Weber number

$$W_c = \frac{\rho U_{rel}^2 \overline{D}}{\sigma} \tag{2.94}$$

in combination with the collector and the smaller droplet radius is used to define critical offset and thus the outcome of the collision. Namely, it is either bouncing or coalescence for the droplets with Weber number under 100. For the values above that the outcome of droplet collision can be shattering.

O'Rourke [O'Rourke et al., 1989] collision model calculates collision probability of a collector with the smaller droplet, so that the larger droplet (collector) is set as frame of the reference for the calculation with the zero velocity.

The collision volume is defined as the area around the collector droplet multiplied by the distance traveled by smaller droplet in a time step:

$$V_C = \pi(r_1 + r_2)^2 v_{rel} \Delta t \tag{2.95}$$

If the particle is within the cell with volume V in the continuous phase, the colliding probability is given as the ratio of two volumes:

$$P = \frac{\pi(r_1 + r_2)^2 v_{rel} \Delta t}{V} \tag{2.96}$$

The mean expected number of collisions in generalized form considering collector and smaller parcel with n_1 and n_2 number of parcels is calculated as:

$$\overline{n} = n_2 \frac{\pi (r_1 + r_2)^2 v_{rel} \Delta t}{V} \tag{2.97}$$

The number of actual collision encounters is not the expected mean number of collisions, but corresponds to Poisson probability distribution that collector undergoes n number of collisions calculated for every parcel pair, which is given by:

$$P(n) = e^{-\overline{n}} \frac{\overline{n}^n}{n!} \tag{2.98}$$

In the last step a random sample from the Poisson distribution is used to detect eventual collision pairs. Obviously, for $n = 0$ there is no collision between parcels with a corresponding probability $P(0) = e^{-\overline{n}}$. For randomly chosen number X between 0 and 1 if condition $X < P(0)$ is true there is no collision. For $X > P(0)$ the next random number Y in the same interval is used to determine if the outcome is coalescence or grazing collision causing change in particle velocity vector, as in the last case the other properties are not altered. Mathematical procedure to determine if the outcome of the collision is coalescence or grazing and calculation of droplet velocity components can be found in the literature.[O'Rourke et al., 1989],[Josef, 2010],[Ansys Inc, 2013].

2.2.2.8 Droplet break up model

Aerodynamic interaction between droplet and surrounding gas leads to deformation due to oscillation and distortion and in the last consequence to droplet break up which is known as secondary breakup or atomization.

One of the most used models applicable to broad spectrum of engineering problems is Taylor Analogy Breakup (TAB) model. TAB model is based on mathematical formulation of mass-spring system for a dumped harmonic oscillator with external excitation:

$$m\ddot{x} + d\dot{x} + kx = \mathbb{F}, \tag{2.99}$$

where m, d, k and $\mathbb{F}$ are mass, damping constant, spring constant and force, respectively.

In TAB model the external excitation force corresponds to the superposition of impact and aerodynamic force, damping force is effect of fluid viscosity and restoring force acting in direction of equilibrium is analogous to surface tension force. Dividing Equation 2.99 by m, in accordance with the Taylor analogy the respective conceptual physical formulation of coefficients is:

$$\begin{aligned} \frac{F}{m} &= \mathbb{C}_F \frac{\rho_g u^2}{\rho_l r_0} \\ \frac{k}{m} &= \mathbb{C}_k \frac{\sigma}{\rho_l r_0^3} \\ \frac{d}{m} &= \mathbb{C}_d \frac{\mu_l}{\rho_l r_0^2} \end{aligned} \tag{2.100}$$

In the equation above ρ stands for density, μ for viscosity, with index g and l for gas and liquid respectively, σ is surface tension coefficient and r_0 is radius of undeformed droplet as shown in Figure 2.17.

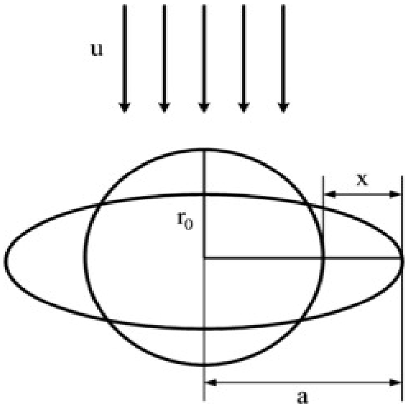

Figure 2.17: Drop deformation scenario used in the TAB model [O'Rourke and Amsden, 1987]

Values for modeling constants are given in Table 2.4. It is obvious that droplet break up occurs if and only if the oscillation amplitude of the droplet pole reaches value of the droplet radius.

$\mathbb{C}_F$	$\mathbb{C}_k$	$\mathbb{C}_d$
1/3	8	5

Table 2.4: Dimensionless constants of Taylor Analogy Model

The given formulation of the linear differential equation is valid for all Weber numbers, implemented numerical solution method can be found in the recommended literature.[O'Rourke and Amsden, 1987],[Lee et al., 2012]

2.2.2.9 Discrete Element Method Collision Model

Discrete Element Method (DEM) as a part of DPM is used to simulate mechanical interaction between particles of granular matter, calculating resulting force on contact points. Resulting force is estimated using linear spring collision law. Direction of reacting force is determined by unity vector at contact point defined by particle position:

$$\vec{e}_{12} = \frac{x_2 - x_1}{\| x_2 - x_1 \|} \tag{2.101}$$

where x_1 and x_2 represent coordinates of colliding particles. At the colliding point, particle volumes overlap during the contact :

$$\delta = \| x_2 - x_1 \| - (r_1 + r_2). \tag{2.102}$$

It is obvious from the equation above that overlap δ during collision time has negative value. Reacting force is calculated using spring constant K:

$$\vec{F}_1 = K\delta\vec{e}_{12}, \tag{2.103}$$

which is given by following relation:

$$K = \frac{\pi u_{rel}^2 D\rho}{3\epsilon_D^2}. \tag{2.104}$$

Maximum overlap is defined by the fraction of diameter ϵ_D, u_{rel} is relative velocity of colliding particles, D is diameter and ρ stands for particle density. [Cundall and Strack, O. D. L., 1979],[Ansys Inc, 2013]

2.2.2.10 Turbulent dispersion

There are two basic models for the prediction of particle dispersion under the influence of turbulence in the fluid phase, particle cloud model and stochastic tracking model (random walk).
The cloud model predicts the statistical propagation of the particle concentration in a expanding cloud around a mean trajectory by Gaussian probability density function, making it suitable for spray propagation.
In the stochastic discrete random walk model approach, particle trajectory is evaluated using mean flow velocity and additionally influence of a fluctuating part caused by turbulent eddies. This model is not suitable for strongly non-homogeneous diffusion driven flows and for prediction of wall impact rate of micron size particles caused by turbulence. Further details on mathematical modeling of turbulent dispersion can be found in the literature references. [Baxter and Smith, 1993].[Guangyuan Sun, 2015],[Ansys Inc, 2013]

2.2.2.11 Heat Transfer

The existing temperature difference between moving particle and fluid is driving force for the convective heat transfer and radiation on the particle surface.
Furthermore, for the small particles it can be assumed that effect of internal resistance is negligible, which leads to following expression for the heat transfer between particle and fluid:

$$m_p c_p \frac{dT_p}{dt} = \alpha A_p (T_\propto - T_p) + \epsilon_p A_p \sigma (\Theta_R^4 - T_p^4), \tag{2.105}$$

where m_p stands for mass of the particle, $T_\propto$ is local continuous phase temperature, T_p particle temperature, c_p particle heat capacity, A_p surface area of the particle, α heat transfer coefficient, σ Stefan-Boltzman constant, ϵ_p dimensionless particle emissivity and Θ_R^4 stands for radiation temperature.

Incident radiation G (in W/m^2) is calculated as integral value of the radiation intensity $\mathbb{I}$ over the solid angle $\Omega = 4/pi$:

$$G = \int\limits_{\Omega} \mathbb{I} d\Omega \tag{2.106}$$

Assuming that particle temperature change is linear, i.e. temperature change within a time step is small, Equation 2.105, which is supposed to be integrated over the time, can be written as:

$$m_p c_p \frac{dT_p}{dt} = A_p \Big\{ - \Big[\alpha + \epsilon_p \sigma T_p^3\Big] T_p + \Big[\alpha T_\propto + \epsilon_p \sigma \Theta_R^4\Big] \Big\} \tag{2.107}$$

After computation of particle position using Equation 2.85 and Equation 2.87, particle temperature at the following time step can be calculated using following equation:

$$T_p(t+\Delta t) = a + [T_p(t) - a]e^{-b\Delta t} \tag{2.108}$$

where

$$a = \frac{\alpha T_\propto + \epsilon_p \sigma \Theta_R^4}{\alpha + \epsilon_p \sigma T_p^3(t)} \tag{2.109}$$

and

$$b = \frac{A_p\Big(\alpha + \epsilon_p \sigma T_p^3(t)\Big)}{m_p c_p} \tag{2.110}$$

The heat transfer on spherical particle can be described by known dimensionless Ranz-Marshall correlation:

$$Nu = \frac{\alpha d_p}{\lambda} = a + bRe^m Pr^n \tag{2.111}$$

with

$$Pr = \frac{\mu}{cp\lambda} \tag{2.112}$$

where Nu is Nusselt number that characterize thermal boundary layer,α is the heat transfer coefficient and λ thermal conductivity of the gas; Pr stands for Prandtl number of surrounding gas. Particle Reynolds number Re is given by Equation 2.92.

The constants a,b,m,n are dependent on the fluid characteristics and flow geometry. There are numerous numerical correlations for the constants available in the literature, dependent on the problem set up. The values used in this work are given in the following table:

a	b	m	n
2	0.6	1/2	1/3

Table 2.5: Empirical constants for calculated Nusselt number

For the case that working temperature reaches droplet/particle boiling point, it is necessary to extend problem definition for the latent heat term. Under atmospheric pressure condition latent heat variation can be assumed negligibly small. Otherwise for variable pressure, the changing latent heat has to correspond with the boiling temperature and average pressure in the area of influence on the particle surface. Considering latent heat in heat balance equation leads to a modified formulation of Equation 2.105:

$$m_p c_p \frac{dT_p}{dt} = \alpha A_p (T_\propto - T_p) + \epsilon_p A_p \sigma (\Theta_R^4 - T_p^4) - \frac{dm_p}{dt} h_f g \tag{2.113}$$

where dm_p/dt represents evaporation rate in kg/s. In general, mass flux of vapor from the droplet to surrounding gas depends on driving concentration gradient, which is explained in detail in Mass Transfer section.[Clift et al., 2013],[Ansys Inc, 2013]

2.2.3 Mass Transfer and Reaction Kinetics

2.2.3.1 Mass Transfer

Following literature has been used as information source for this section : [Boyadjiev, 2014],[Krishna and Wesselingh, 1997],[Lewis and Whitman, 1924],[Michaelides, 2006],[Francis and Allan, 2007].

The principle underlying the physical process of mass transfer mechanism is non equilibrium condition between different phases or concentration gradient within a single phase.

Mass transfer phenomenon is analogous to chemical reaction equilibrium, i.e. in the equilibrium state forward and reverse reaction rate are equal and there is no net measurable change in the concentration with time.

Mass transfer equation for diffusive and advective transport are exactly the same, whereby temperature variable is replaced by concentration and thermal diffusivity by mass transfer diffusivity. Diffusion mechanism occurs in solids, stationary media and in the boundary layers between the phases.

Implementation of the component mass with a nonuniform concentration in the Equation 2.2 substituting elementary volume mass with ρc leads to:

$$\frac{\partial \rho c}{\partial t} + \nabla(\rho c \cdot \mathbf{v}) = 0 \tag{2.114}$$

where c is concentration of the component per unit mass of the fluid. Hence, the mass transfer over the closed surface of defined volume region is result of the molecular diffusion due to motion of nonuniform distribution and motion caused by convective transport over the surface. Concentration distribution nonuniformity causes diffusive mass flux over the surface that encloses control volume, which is described by Fick's first law:

$$\mathbf{q_c} = -\mathbb{D}\nabla(\rho c) \tag{2.115}$$

where $\mathbb{D}$ molecular diffusion coefficient. Implementing divergence of mass flux into mass balance defined in Equation 2.114 leads to convection-diffusion equation:

$$\frac{\partial \rho c}{\partial t} + \nabla(\rho c \cdot \mathbf{v}) + \nabla \mathbf{q_c} = 0 \tag{2.116}$$

which in combination with Equation 2.115, assuming $\mathbb{D}$ and ρ constant, can be written in following form:

$$\frac{\partial c}{\partial t} + \nabla(c \cdot \mathbf{v}) = \mathbb{D}\nabla^2 c \tag{2.117}$$

For the stagnant fluid the above equation reduces to Fick's second law:

$$\frac{\partial c}{\partial t} = \mathbb{D}\nabla^2 c \tag{2.118}$$

Mass transfer in turbulent flow is result of small-scale turbulent motion which is analogue to molecular diffusion and large-scale turbulent pulsation which leads to turbulent diffusion in the fluid flow. Therefore, turbulence significantly increases diffusion effect in a streaming medium, which means that the only difference to laminar flow is the diffusivity.

In the near wall region, due to velocity decrease and consequent decrease in turbulent intensity, turbulent diffusion depends on the wall distance and mass transfer rate is limited by the diffusion sublayer.

In gas-liquid binary composition the system tends to achieve an equilibrium state, so if the liquid is not saturated with the gas under given condition, absorption phenomena occurs. The escape of gas, in the case that fluid is supersaturated, can be considered as reverse process, i.e. negative absorption. In the contact region of two phases, on the the gas side develops a layer where the convective mixing rate is negligible compared to main gas region. Similarly, on the fluid side of the interface there is a layer without influence of the mixing caused by convection. Which means that existing surface films are totally free of convective transport and exclusively influenced by diffusion. Convective transport, in this case, causes uniform concentration of the solute in the solvent.

Diffusion on the gas side of the film is directly proportional to the concentration difference of the gas in the film and outer region. On the other hand, diffusion rate on the liquid side depends on the concentration difference between inner region and concentration on the interface. As the film thickness is very small, concentration of the solute within it is negligibly small compared to transferred rate of the solute, which means that mass transfer through resistance films on the both sides can be considered equal.

The resistance to diffusion occurs due to molecular collision which is cause of the greater density of liquids and accordingly greater on the liquid film side. Even though the ratio of the viscosity to density is greater for the gases, consequently is the film thickness causing additional mass transfer barrier grater on the gas side, the main diffusion resistance arises due to collision effect.

Figure 2.18 illustrates described two film model:

Mass transfer rate of the solute is proportional to the interface surface area, diffusion coefficient per unit area and concentration difference between interface and region outside of liquid and gas film as a driving force:

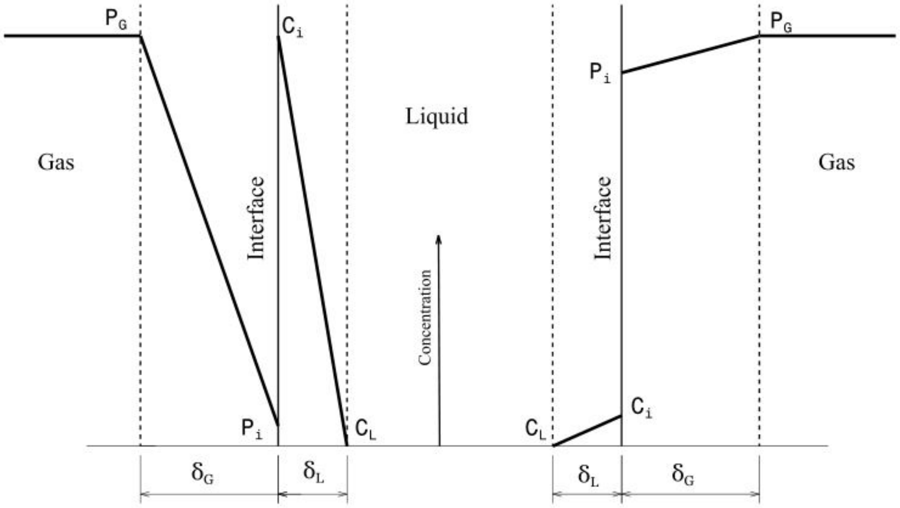

Figure 2.18: Mass Transfer

$$\frac{dm}{Adt} = k_g(P_G - P_i) = k_L(C_i - C_L) \tag{2.119}$$

Here,k_g and k_L are diffusion rate coefficients on the gas and liquid side known as mass transfer coefficients, C is concentration of the gas compound on the liquid side of the gas-liquid interface, P is concentration on the gas side, subscripts i,G and L stand for interface, gas and liquid respectively and A is reference surface. Depending on the solubility of the solute there is distinction between three different cases : very soluble gases, slightly and intermediate soluble gases. For the extreme cases the main resistance to absorption is determined either by the diffusion rate through the gas film for very soluble gas or through the liquid film for slightly soluble gas, so that the resistance on the other side of interface can be neglected.

For a general case of intermediate solubility we assume that the Henry's law holds for the given concentration range. Henry's law is given as:

$$C = HP, \tag{2.120}$$

where H is Henry constant, C and P refer to the concentration of the gas component in the liquid and gaseous phase, respectively.

From the Equation 2.119, Equation 2.120 and ideal gas equation after some algebraic transformation follows:

$$\frac{dm}{Adt} = K_G(P_G - P_L) = K_L(C_G - C_L) \tag{2.121}$$

with

$$K_G = \frac{Hk_Lk_G}{Hk_L + k_G} \tag{2.122}$$

and

$$K_L = \frac{K_G}{H} = \frac{k_Lk_G}{Hk_L + k_G} \tag{2.123}$$

It should be considered that the Henry's law is in general applicable only over the narrow temperature range and depends on the pressure and the type of the solvent. The Henry's constant increases in the lower temperature range and after reaching maximum, decreases in the higher temperature range. Even small temperature differences of 10-20K can cause change of constant for factor 2-3, dependent on specific mixture pair.

Extrapolation of Henry coefficient from a known value at given temperature $H_i(T_0)$ to temperature T_1 can be done using following relation:

$$\frac{H_i(T_1)}{H_i(T_0)} \approx \frac{\gamma_i^{inf}(T_1)p_i^{sat}(T_1)}{\gamma_i^{inf}(T_0)p_i^{sat}(T_0)} \tag{2.124}$$

Temperature dependence of infinite dilution activity coefficient γ_i^{inf} near the ambient temperature is negligibly small, so that change of H_i is primarily affected by the variation of vapor pressure p_i^{sat}. In that case Equation 2.124 can be simplified to:

$$\frac{H_i(T_1)}{H_i(T_0)} \approx \frac{p_i^{sat}(T_1)}{p_i^{sat}(T_0)} \tag{2.125}$$

The temperature dependency of vapor-pressure $p_i^{sat}(T)$ is experimentally determined for many solutes, whereas data for infinite dilution activity coefficient are rarely available.

An alternative approach for temperature dependency estimation of Henry's coefficient that uses solute enthalpy ΔH_sol is known as Vant's Hoff extrapolation:

$$\frac{H_i(T_1)}{H_i(T_0)} \approx exp\Big[\Big(\frac{\Delta H_{sol}}{R}\Big)\Big(\frac{1}{T_1} - \frac{1}{T_0}\Big)\Big] \tag{2.126}$$

This approximation provides good results for temperature differences of perhaps 20K, which is dependent on solute-solvent pair. Applicable temperature range can be even extended if the heat capacity for solutes are known, so that temperature dependency of solutes enthalpy ΔH_{sol} can be taken into consideration.
Henry's law is used to describe equilibrium state of a soluble species between two phases:

$$[NH_3]_{Gas} \longleftrightarrow [NH_3]_{Aqueous}$$

However, in the aqueous phase partitioning of the ionized molecules occurs:

$$[NH_3]_{Aqueous} + [H_2O] \longleftrightarrow [NH_4^+] + [OH^-].$$

Partitioning of the solute in the aqueous phase in the presence of additional chemical reactions which include any of dissociated species enlarges absorption and the amount predicted by Henry's law is smaller. Analogously, the concentration of the solute in the gaseous phase at equilibrium will be smaller then predicted.
Important factor that influences absorption, as can be seen from the above equations, is mass transfer coefficient which depends on the character of the absorption process.
If the limiting factor is diffusion trough gas film, any factor such as streaming gas velocity that reduces film thickness on the gaseous side will enhance absorption process.
On the other hand, if the absorption is controlled by liquid film thickens, which is the case by slightly soluble gasses, the agitation of the fluid increases absorption rate.
Increased temperature leads to a lower viscosity on the liquid side and in the last consequence decreased liquid film thickness increasing mass transfer rate coefficient k_l. On the other hand, absorption controlled by gaseous film thickness decreases with higher temperature as the density to viscosity ration for the gases decreases.
For less soluble gas an apparatus with gas bubbles dispersed in liquid would lead to a higher mass transfer rate due to continuous exposure to the fresh liquid film, whereas gaseous film has relatively constant characteristics.
Dispersed droplets in gaseous environment is the apparatus concept for very soluble medium, as it provides possibility to influence gas film thickness.
Mass transfer coefficient is, similarly to heat transfer coefficient, calculated from Sherwood correlation, where the Sherwood number is given as :

$$Sh = \frac{kd_p}{\mathbb{D}} = a + bRe_p^m Sc^n, \tag{2.127}$$

where Sc is Schmidt number defined as :

$$Sc = \frac{\mu}{\rho\mathbb{D}}, \tag{2.128}$$

$\mathbb{D}$ stands for diffusion coefficient in surrounding medium and a,b,m,n are constants. Numerical values for the model constants suitable for spray calculations are given in Table 2.6:

a	b	m	n
2	0.6	1/2	1/3

Table 2.6: Empirical constants for calculated Sherwood number

As for the Nusselt number, there are numerous empirical Sherwood correlations from diverse authors describing absorption phenomena based on data from different experimental set ups, which has to be taken into consideration by the choice of the appropriate formulation. If the particle reaches vaporization temperature mass transfer to the gaseous phase is driven by vapor concentration gradient between particle surface and surrounding gas:

$$N_i = k(P_{i,s} - P_{i,\infty}), \tag{2.129}$$

where N_i is vapour molar flux, k is mass transfer coefficient calculated from Equation 2.128, $P_{i,s}$ vapor concentration on droplet/particle surface and $P_{i,\infty}$ vapor concentration in the bulk gas. Under assumption that the partial pressure at the interface corresponds to the saturation vapor pressure by the particle temperature, vapor concentration on the surface is computed by following equation:

$$P_{i,s} = \frac{p_{sat}(T_p)}{RT_p} \tag{2.130}$$

Vapor concentration in the surrounding gas is obtained from the equation:

$$P_{i,\infty} = \frac{X_i p}{RT_\infty} \tag{2.131}$$

with X_i as local mole fraction of the component in bulk gas, p stands for absolute pressure and T_∞ is gas temperature. Change in droplet/particle mass is calculated in every time step:

$$m_p(t + \Delta t) = m_p(t) + N_i A_p M_i \Delta t \tag{2.132}$$

where A_p is particle surface and M_i stands for molecular weight of the component i.

The equation above is solved coupled with the equivalent heat transfer equation for the particle with variable mass.

Formulation of mass transfer model based on Fick's is valid under following conditions:

- system consists of binary mixture
- one species is diluted in an multicomponent mixture
- there are no other additional force fields of influence such as electrostatic or centrifugal
- there are no cross-effects (reverse or osmotic diffusion)

The Maxwell-Stefan approach enables description of multicomponent systems based on molecular balance with possibility to model therms for additional forces. Still, it is quite complex model for numerical implementation which needs extra effort for determination of diffusion coefficients for multicomponent systems.

Stefan convection

Experimental studies showed that the change of fluid viscosity influenced by mass transfer from the drops can be approximated using reference viscosity for the estimation of transport coefficients, which given by following equation:

$$\mu_{ref} = \mu_s + \frac{1}{3}(\mu_\infty - \mu_s) \tag{2.133}$$

where μ_s represents fluid viscosity at the sphere surface and μ_∞ viscosity of the fluid phase far from sphere. This correction equation for the viscosity, which is experimentally confirmed by several authors, can be used for correction of the standard drag curve for ellipsoidal drops if the relative ratio of the axes doesn't exceed 10%. The effective diameter of the ellipsoid used for the calculation:

$$d_{eff} = \sqrt[3]{a^2 b} \tag{2.134}$$

with a as major and b as minor axis of the ellipsoid.

For vaporization rate $B_T \leq 3$, with

$$B_T = \frac{(T_\infty - T_s)}{L}, \tag{2.135}$$

where T_∞ stands for fluid temperature at the sphere surface, T_∞ temperature of the surrounding fluid far from sphere surface and L is characteristic length, standard drag coefficient of a droplet may be used. In this case, reference temperature T_{ref} and reference concentration Y_{ref} are estimated using 1/3 rule:

$$\begin{aligned} T_{ref} &= T_s + \frac{1}{3}(T_\infty - T_s) \\ Y_{ref} &= Y_s + \frac{1}{3}(Y_\infty - Y_s) \end{aligned} \tag{2.136}$$

[YUEN and CHEN, 1976]

For high vaporization rates mass transfer from the particle or droplet surface causes significant change in the boundary layer.

The effect of the convective flow between particle or droplet surface and bulk gas induces change in transport properties through:

- change of thermophysical properties, especially viscosity, due to temperature and concentration gradient change
- reference surface area of droplet changes with variable mass
- convective flow induces weak radial velocity field
- influence on drag coefficient

Mass evaporation and Stefan convection tend to reduce drag force, which makes it necessary to define correction therm for drag coefficient.

Eisenklam [Eisenklam et al., 1967] proposed following correlation for drag coefficient correction based on experimental studies:

$$C_D = \frac{C_{D,0}}{1 + B_m} \tag{2.137}$$

where $C_{D,0}$ stands for initial drag coefficient obtained without mass transfer. Blowing coefficient B_m, sometimes referred to as Spalding number, takes into account mass fraction of vapor on the droplet surface and in surrounding medium:

$$B_m = \frac{Y_s - Y_\infty}{1 - Y_s} \tag{2.138}$$

Accordingly, droplet mass change rate is evaluated using following relation:

$$\frac{dm_p}{dt} = kA_p\rho_\infty(1 + B_m) \tag{2.139}$$

Analogously, mass flow of the phase change influences heat transfer from the particle. Therefore, modified Nusselt number is used for computation of heat transfer coefficient:

$$Nu = \frac{\alpha d_p}{\lambda} = \frac{ln(1 + B_m)}{B_m}(2 + 0.6Re_p^{1/2} + Pr^{1/3}) \tag{2.140}$$

Blowing effect is an important issue considering heat transfer from the particle with corresponding mass transfer at its surface, in the case that time scale of the mass transfer is of equal or lesser magnitude then the time scale of the energy transfer. Which means, that the correction coefficient for the heat transfer has to be implemented if it is of equal magnitude or fast in comparison to mass transfer process.

The functional forms of the equations for the correction factors recommended from different authors based on the experimental study are very similar and yield often results correct to a few percentages.

For the simple cases, in the absence of more accurate information, viscous spheres can be approximated by adequate formulation for rigid sphere, which yields fairly accurate prediction. If the transient and aggregation effects are of the same order of magnitude, time-average quantities are sufficient for the approximation. For higher accuracy, especially for the complex systems, it is unavoidable to define proper transport coefficients.[Michaelides, 2006],[Aggarwal and Peng, 1995]

2.2.3.2 Diffusion coefficient

Diffusion coefficient is an important parameter used to describe how fast the substances in binary system diffuse into each other. When diffusion coefficient is known total mass transport can be calculated from the Equation 2.115.

Most of the diffusion coefficient models are based on Chapman-Enskog hard sphere model:

$$\mathbb{D}_{AB} = \frac{3}{32n\sigma_{AB}^2}\left[\frac{8kT}{\pi}(1\backslash M_A + 1\backslash M_B)\right]^{1\backslash 2} \tag{2.141}$$

In the equation above n stands for the total concentration of both species, T is the temperature in K, k Boltzmann constant, $M_{A,B}$ is molecular mass and σ_{AB} is collision diameter i.e. distance between molecular centers upon collision where $\sigma_{AB} = \frac{1}{2}(\sigma_A + \sigma_B)$.

The limitations of this model are temperature dependence to power of 3\2 which doesn't correspond to experimental observations and very few available σ values that are additionally only valid for narrow temperature ranges.

For prediction of binary gas phase diffusion Fuller [Fuller et al., 1966] derived following half-empirical temperature and pressure dependent correlation neutralizing physical and mathematical restrictions of the other models:

$$\mathbb{D}_{AB} = \frac{1.013 \cdot 10^{-7} T^{1.075} (1 \backslash M_A + 1 \backslash M_B)^{1 \backslash 2}}{p \Big[(\Sigma_A v_A)^{1/3} + (\Sigma_B v_B)^{1/3} \Big]} \tag{2.142}$$

where C and b are arbitrary constants, p is pressure, T temperature, $v_{A,B}$ diffusion volume and $M_{A,B}$ is molar mass of the individual component. Here, the diffusion volume is a special parameter with assumed additive characteristics.

Model constants are calculated by authors using non-linear least squares analysis from the experimental data for bright range of binary systems.

It has to be noted that the model developed by authors is fully reliable only for the systems used for method development. Otherwise it has to be compared with experimental data or some more reliable theoretically based method.

Table 2.7: Atomic and Structural Diffusion Volume Increments.

C	16.5	(Cl)	19.5
H	1.98	(S)	17.0
O	5.48	Aromathic or Hetero-cyclic rings	-20.2
(N)	5.69		

Table 2.8: Diffusion Volume of Simple molecules.

H_2	7.07	CO_2	26.9
D_2	6.70	N_2O	35.9
He	2.88	NH_3	14.9
N_2	17.9	H_2O	12.7
O_2	16.6	(CCl_2F_2)	114.8
Air	20.1	(SF_6)	69.7
Ne	5.59		
Ar	16.1	(Cl_2)	37.7
Kr	22.8	(Br_2)	67.2
(Xe)	37.9	(SO_2)	41.1
CO	18.9		

Diffusion volume increments listed in Table 2.7 are to be used for the systems with organic vapors, whereas diffusion volume for simple molecules can be taken from Table 2.8[2].[Fuller et al., 1966]

2.2.3.3 Chemical Reactions

Overall chemical reaction in general is given by chemical equation:

$$\nu_A A + \nu_B B + ... \leftrightarrows \nu_F F + \nu_G G + ..., \sum_i \nu_i P_i = 0 \tag{2.143}$$

where ν_i is stoichiometric coefficient which is negative for reactants and P_i stands for the i_{th} the chemical component. According to Hess' law of constant heat summation, enthalpy change of a chemical reaction is pathway independent and standard enthalpy of reaction $\Delta_R H^0(T^0)$ is equal to the sum of standard enthalpy of formation $\Delta_F H^0(T^0)$ for each component on reactant's and product's side:

$$\Delta_R H^0(T^0) = \sum_i \nu_i \Delta_F H^0(T^0). \tag{2.144}$$

Temperature dependency of enthalpy change for known specific heat capacity function for a given temperature range, according to Kirchhoffs' law, is given by:

$$\Delta_R H^0(T) = \sum_i \nu_i \Delta_F H^0(T^0) + \sum_i \nu_i \int_{T^0}^{T} c_p(T) dT \tag{2.145}$$

Analogously to enthalpy, standard reaction entropy $\Delta_R S^0(T^0, p^0)$ is equal to the sum of standard enthalpy of formation $\Delta_F S^0(T^0, p^0)$ for each component and can be written as:

$$\Delta_R S^0(T^0, p^0) = \sum_i \nu_i \Delta_F S^0(T^0, p^0) \tag{2.146}$$

Considering temperature dependency, standard reaction entropy for given pressure p and partial pressure p_i of the component we obtain:

$$\Delta_R S(T, p^0) = \Delta_R S^0(T^0, p^0) + \sum_i \nu_i \int_{T^0}^{T} \frac{c_p(T)}{T} dT + R \sum_i \nu_i ln \frac{p_i}{p^0} \tag{2.147}$$

Equations above are used for the calculation of free standard reaction enthalpy, also know as Gibbs free energy or Gibbs function, under consideration of temperature and pressure change dependency:

$$\begin{aligned} \Delta_R G^0(T, p^0) &= \Delta_R H^0(T) + T \Delta_R S(T, p^0) \\ \Delta_R G^0(T, p^0) &= \sum_i \nu_i \Delta_F G^0(T, p^0) \\ \Delta_R G(T, p) &= \Delta_R G^0(T, p^0) + RT \prod_i ln \Big(\frac{p_i}{p_0}\Big)^{\nu_i}, \end{aligned} \tag{2.148}$$

---

[2] () indicates that listed value is based on only a few data points

A significant fact that follows from the definition of Gibbs free energy is that its change equals to zero for the system in equilibrium state and decreases, i.e. the change is negative, upon the occurrence of chemical reactions.
Hence, thermodynamic equilibrium state constant can be defined as:

$$K(T) = e^{-\frac{\Delta_R G^0(T,p^0)}{RT}} = \prod_{i=1}^{k} \Big(\frac{p_i}{p_0}\Big)^{\nu_i}, \tag{2.149}$$

where the partial pressure of the component is defined as:

$$p_i = \nu_i * p, \tag{2.150}$$

with distinction between products (indices p) and reactants (indices r) components, equilibrium constant can be written as:

$$K(T) = \Big(\frac{p}{p_0}\Big)^{\sum_{i=1}^{k} \nu_i} \frac{\prod_{i=1}^{k} \nu_{i,p}^{\nu_{i,p}}}{\prod_{i=1}^{k} \nu_{i,r}^{|\nu_{i,r}|}}, \tag{2.151}$$

For the liquid mixtures and solutions, using molar concentration of the component $[C_i]$ instead of partial pressure, equilibrium constant can be expressed as:

$$K_c(T) = e^{-\frac{\Delta_R G^0(T,p^0)}{RT}} = \prod_{i=1}^{k} [C_i]^{\nu_i} \tag{2.152}$$

In the case of ideal gas mixtures conversion between K and K_c can be calculated directly using ideal gas equation:

$$\begin{gathered} p_i V = n_i R_m T \Rightarrow p_i = [C_i] R_m T \\ K(T) = \prod_{i=1}^{k} \Big(\frac{p_i}{p_0}\Big)^{\nu_i} = K_c(T) \prod_{i=1}^{k} \Big(\frac{R_m T}{p_0}\Big)^{\nu_i} = K_c(T) \Big(\frac{R_m T}{p_0}\Big)^{\sum_{i=1}^{k} \nu_i}, \end{gathered} \tag{2.153}$$

Under real condition, the interaction between components causes discrepancy compared to an ideal state. A measure of this effective non-ideal state is called activity a_i, which depends on pressure, temperature and composition of the solution. Relation of the activity to the ideal state is quantified by correctional activation coefficient γ_i:

$$a_i = \gamma_i [C_i] = \gamma_i \frac{p_i}{p_0}. \tag{2.154}$$

Hence, the equilibrium constant K_a can be formulated under consideration of the thermodynamic activity:

$$K_a = e^{-\frac{\Delta_R G^0(T,p^0)}{RT}} = \prod_{i=1}^{k} a_i^{\nu_i} \tag{2.155}$$

[Klell, 2012]

2.2.3.4 Reaction Rate Constant

The time evolution of chemical reaction systems (chemical kinetics) is quantified by reaction rate which is negative for reactants and positive for products. For each component i of the chemical reaction it is defined as temporal change of concentration:

$$r_{c_i} = \frac{d[C_i]}{dt} \tag{2.156}$$

Using stoichiometric coefficients from Equation 2.143 and considering mass conservation, reaction rate r can be written as:

$$r = \frac{r_{c_i}}{\nu_i} = \frac{1}{\nu_i}\frac{d[C_i]}{dt} \tag{2.157}$$

In general, reaction rate is pressure, temperature and concentration dependent physical quantity that is usually experimentally determined. Relating to Equation 2.143, it is often found to be of following form:

$$r = k(T) \cdot [A]^a \cdot [B]^b \cdot ... \cdot [F]^f \cdot [G]^g ..., \tag{2.158}$$

with a, b, f, g as reaction order exponents determined by reaction mechanism, that are not necessarily equal to stoichiometric coefficients and $k(T)$ defined as reaction rate constant with temperature dependence that can be estimated by Arrhenius-equation:

$$k = A \cdot e^{-\frac{E_a}{R_m T}}. \tag{2.159}$$

In some cases, temperature dependence of pre-exponential factor A needs to be taken into account using following relation:

$$k = A \cdot T^b \cdot e^{-\frac{E_a}{R_m T}} \tag{2.160}$$

Equilibrium constant can be expressed as ratio of reaction rate constants of the forward (k_f) and reverse (k_r) chemical reaction process:

$$K_c = \frac{k_f}{k_h} \tag{2.161}$$

[Klell, 2012]

2.2.3.5 Mass Transfer with Chemical Reactions

The transport of the solute due to mass transfer mechanism with simultaneous chemical reaction in the liquid phase increases the absorption capacity. Therefore, absorption model has to be expand for an additional term that approximates influence of the chemical reaction in the mass transport mechanism that consists of the following steps:

- transport of the solute to the phase interface
- diffusion through surface film into liquid phase
- transport of the reactant to reaction zone
- chemical reaction and further transport of the products

Resulting increase in the mass transfer coefficient due to presence of chemical reaction is quantified using Enhancement factor E as a ratio between additional chemical and pure physical absorption:

$$E = \frac{k_{L,r}}{k_L} \tag{2.162}$$

There are numerous ways proposed for mathematical description of enhancement factor dependent on the mass transfer model chosen. For the two film model, if the reaction occurs solely in the liquid phase, enhancement factor is identical to Hatta number Ha. For two component (i and j) in a gaseous and liquid phase, with reaction order m_i and m_j and reaction rate constants $k_{i,j}$, Hatta number is expressed as:

$$Ha = \frac{\sqrt{\mathbb{D}_i \frac{2}{m_i} k_{i,j} C_{i,L}^{(m_j-1)} C_{j\infty}}}{k_L} \tag{2.163}$$

In the case of instantaneous reaction on the interface between phases ($3 \leq Ha$) enhanced absorption rate is given as:

$$\frac{dm}{Adt} = k_L \cdot C_{i,L} \cdot Ha \tag{2.164}$$

[Vaidya and Kenig, 2007]

Chapter 3

Numerical principles

3.1 Meshing

Meshing is process of discretization of the calculation domain into small, in a case of three-dimensional mesh, volume elements. Such discrete geometry model with finite-volume calculation approach enables numerical calculation of partial differential equations in respect of conservation laws as described in General Model.
There are three distinctive mesh types : structured unstructured and hybrid combination of previous two.
Usually, three-dimensional structured mesh is built of hexahedral elements, while unstructured mesh is tetrahedral or polyhedral. The interior vertices of a structured, mostly hexahedral meshes, are topologically alike following an uniform pattern with face normals of a volume element intersecting at the center, whereas vertices of unstructured mesh are arbitrarily varying.
Structured hexahedral mesh of a cylindrical geometry used for simulation of lycopodium dispersion is shown in Figure 5.8a. Interior cell arrangement of a segment in a cutting plane normal to y axis is illustrated in Figure 5.8b.

Advantage of a structured domain, especially in a sense of coding and memory usage, is that node locations are functionally related thus neighbor cells are easily and fast accessible. Unstructured mesh disretizes complex geometries more precisely enabling definitions of refinement regions. Additionally, polyhedral unstructured mesh can approximate directional dependencies of fluxes much better, as well as gradient values. The number of cells in this type of mesh after conversion is significantly smaller compared to tetrahedral. Still, some numerical methods are better suitable for one type of mesh then another.

The meshing process for polyhedral mesh is divided into two steps : generation of tetrahedral mesh with refinement for the zones with expected higher field gradients and subsequently conversion into polyhedral mesh.
Tetrahedral mesh generation in ANSYS-ICEM$^{®}$ is based on Delaunay triangulation techniques that creates mesh of nonoverlapping, contigous triangles from the set of discrete points with the constraint that there are no

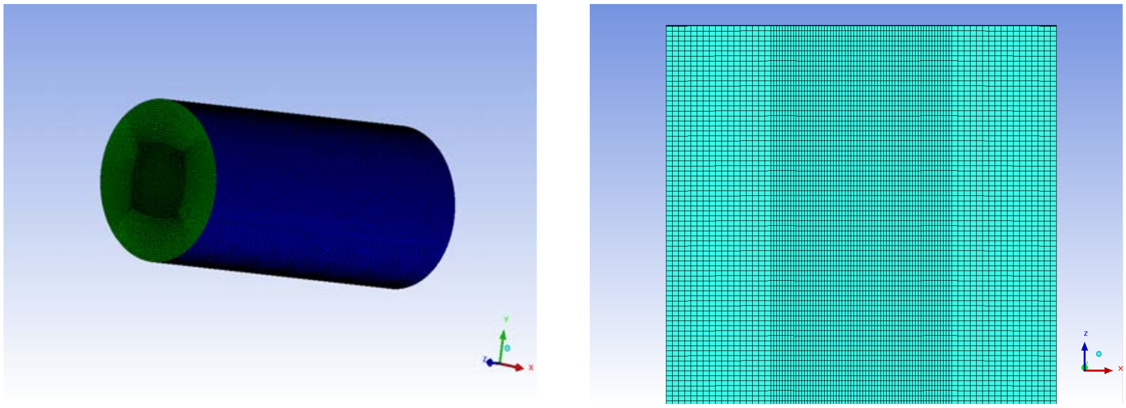

(a) Hexahedral mesh of a cylindrical geometry

(b) Projection on cutting plane

Figure 3.1: Structured hexahedral mesh

vertices lying within the area defined by circumcircle of any triangle.Figure 3.2 illustrates described principle. To avoid possible extremely long edges algorithm maximizes minimum of the interior angle. Conversion of tetrahedral mesh to polyhedral is done in ANSYS-FLUENT®. Beside other advantages mentioned above in this chapter, dependent on the initial geometry, conversion to polyhedral mesh reduces number of cells by factor 3-5.

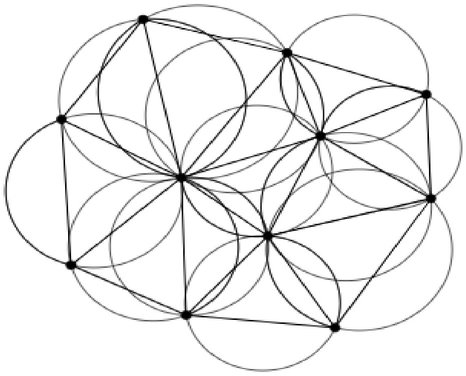

Figure 3.2: Delaunay Triangulation principle

Maximum or minimum mesh and cell size for implicit method discussed in following section is case dependent and there is no accurate predictive model. Grid independence check has to be obtained for every working condition, id est that the final solution doesn't change with further mesh refinement. [Sack and Urrutia, 2008],[Springborn, 2008]

3.2 Discretization

After the set of governing equations is defined on the discretized computational domain, discretization of the equations leads to the system of algebraic equations. For that purpose it is necessary to define numerical schemes for calculation of diverse quantities. Describing in detail all possibilities and characteristics is out of scope of this work, therefore only the main classification will be considered. For further information is referred to literature used in this section: [Moukalled et al., 2016],[Ferziger and Perić, 2002]. Numerical schemes usually have to be specified for following categories:

- first or second time derivatives - $\frac{\partial}{\partial t}, \frac{\partial^2}{\partial t^2},$)
- gradient scheme - (∇)
- divergence schemes - ($\nabla \cdot$)
- laplacian schemes - (Δ)
- interpolation schemes for interpolation of cell to face quantities
- scheme that approximates gradient of the component normal to a cell face

Numerical simulation of the physical quantities approximates values at the cell and face centroids of the meshed geometry. The cell centered variable calculation is currently most used arrangement. It should be noted that discretization error of this arrangement is highly dependent on mesh smoothness and discretization of the diffusion term on non-orthogonal cells.
Dependent on the art of information transported and quantity to obtain, there are two basic numerical solution methods:

- explizit
- implizit

Explicit method evaluates quantities directly from the previously known values without further iterative steps, whereas implicit method is solving coupled set of equations iterative for the variables from the current and later state of the system.Stability criterion, as an indicator whether the given equation system is solvable, for explizit schemes is given by Courant-Friedrichs-Lewy condition:

$$CFL = \Delta t \sum_{i=1}^{n} \frac{u_{x_i}}{\Delta x_i} \leq 1 \tag{3.1}$$

It means that for transient problems it is sufficient to limit the size of the time step to ensure stability. For the implicit methods, stability control can be achieved using under relaxation factor. For some quantity ϕ, relaxation factor for an iterative step is implemented as follows:

$$\phi^{new} = \phi^{old} + R_f(\phi^{predicted} - \phi^{old}) \tag{3.2}$$

If the relaxation factor $0 < R_f < 1$, method is called successive under relaxation and controls stability of the iterative calculation but slows down the convergence of the solution. Ideally, convergence is achieved if there is no change between iterative successive solutions. Practically, solution is converged if the relative change between consecutive iterations is smaller than some vanishing value. For example, recommended value for mass equation is below 10^{-3} and for energy and species below 10^{-6}. Using over relaxation in case that $0 < R_f < 1$ increases convergence rate of solution simultaneously decreasing stability. For the solution of coupled set of non-linear conservation equations described in chapter General Model iterative implizit method was used.

Furthermore, for numerical solution of the partial differential equations characteristic for fluid dynamics, it is necessary to define boundary conditions and thermo-physical constants or functions.
There are numerous types of boundary conditions but the most common are scalar values specified on boundary and implemented directly known as Dirichlet boundary condition, and a flux value known as a Neumann boundary.

3.3 Solving algorithm

Flow chart shown in Figure 3.3 represents implementation of the general model described in Continuous Phase, Discrete Phase andMass Transfer and Reaction Kinetics sections.
After initialization of the meshed geometry with predefined boundary conditions the calculation starts with a new time step. Continuity, impulse, energy equation and chemistry are solved in the Eulerian frame of reference for the continuous phase. In the next step, turbulence modeling is solved using $k-\epsilon$ relizable model and accordingly eddy viscosity is updated. After that follows injection of the dispersed phase in Lagrangian frame calculating all relevant models described in Discrete Phase section coupled with a phase time step of the continuous phase until convergence criterion is reached.

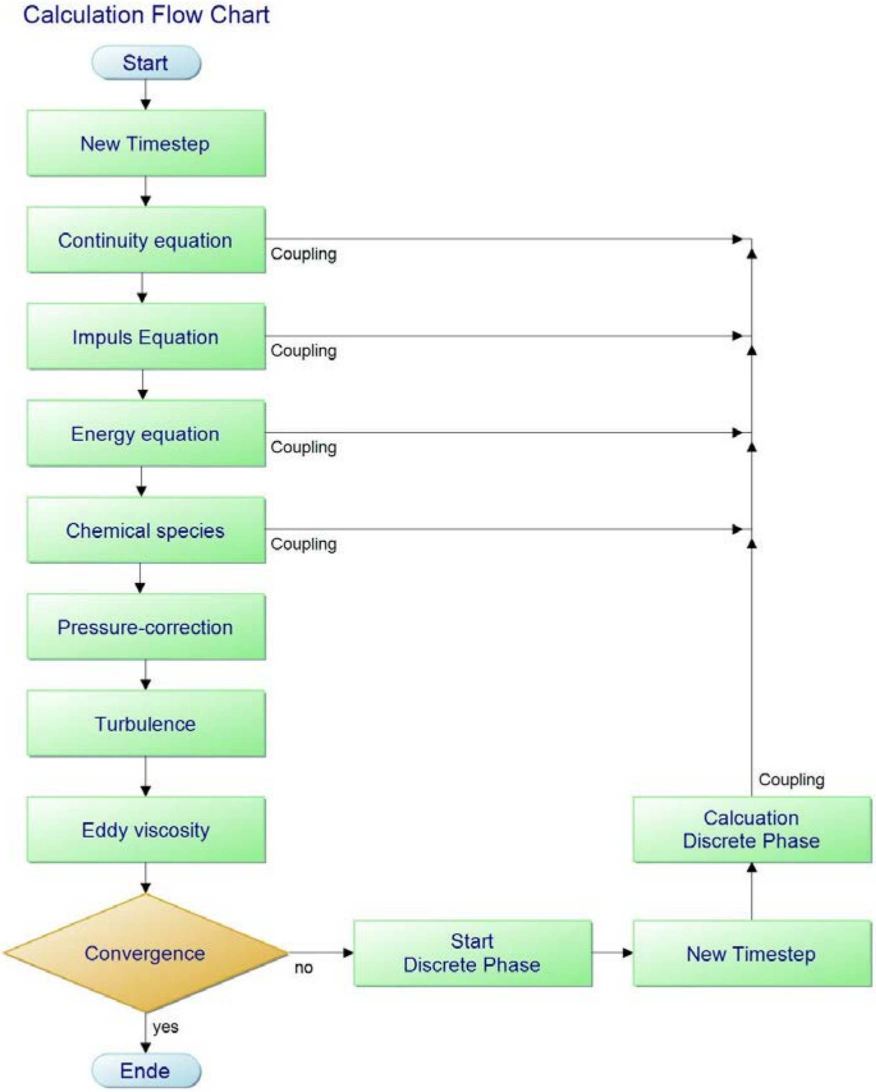

Figure 3.3: Solving algorithm

Chapter 4

Experiments

4.1 Droplet size distribution

Droplet size distribution is the initial condition for the numerical simulation that can be determined either experimentally or modeled mathematically based on maximum entropy principle.

The principle used for the optical droplet size measurement is based on Frauenhofer diffraction of monochromatic light on moving particles, where diffraction pattern is related to the droplet size. Intensity of scattered light is measured using photo diodes and additionally converted into droplet diameters. The limitation of this technique is multiple scattering problem in the dense regions of the spray as the light beam can be scattered by multiple drops. Multiple scattering phenomena leads to broader distribution spectrum and smaller droplet average size.[Lefebvre and McDonell, 2017]

Optimum measuring range of the sensor used for the experimental particle size analysis is between $9\mu m$ and $3500\mu m$. The measurement has been performed for various pressure conditions and resulting mass flows.[Kittinger and Lubensky, 2014]
Experimental set up is shown in Figure 4.1.

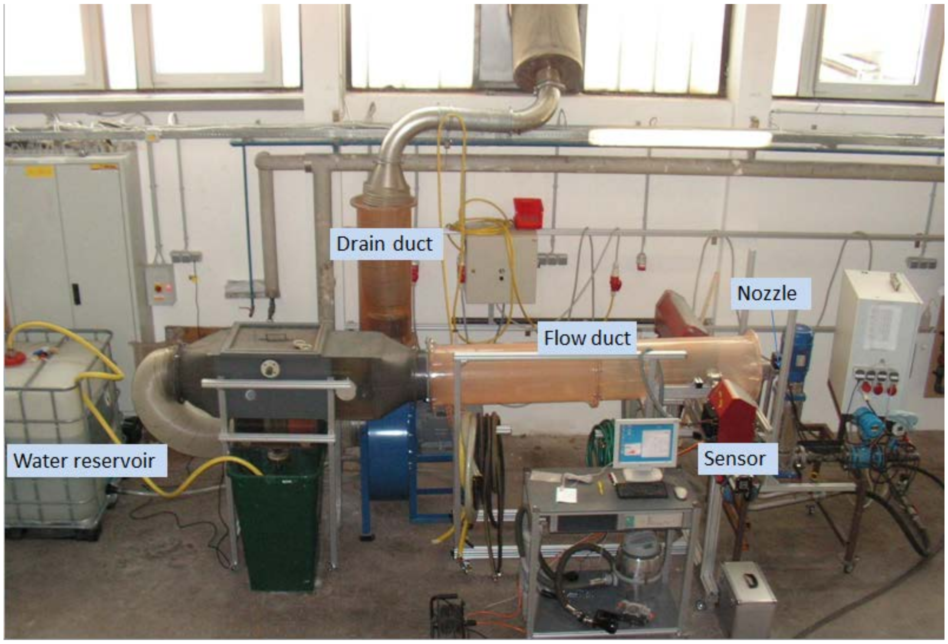

Figure 4.1: Experimental set up - Droplet Size Distribution [Kittinger and Lubensky, 2014]

The overall measurement results are summarized in Table II.

$Q3$	p	V	p	V	p	V	p	V	p	V	p	V	p	V	p	V	p	V
	4.0	0.60	5.0	0.66	6.0	0.71	7.1	0.76	8.0	0.81	9.3	0.87	10.1	0.9	10.8	0.93	11.9	0.97
	[bar]	[l\s]	[bar]	[l\s]	[bar]	[l\s]	[bar]	[l\s]	[bar]	[l\s]	[bar]	[l\s]	[bar]	[l\s]	[bar]	[l\s]	[bar]	[l\s]
0.05	321.1		264.8		247.5		203.7		188.8		149.8		149.8		138.7		128.6	
0.1	422.8		357.7		345.7		283.9		269.0		215.4		214.0		198.9		186.9	
0.15	505.8		432.3		428.9		352.1		335.8		275.5		269.7		252.9		237.2	
0.16	521.4		445.9		444.1		365.3		348.6		287.4		280.4		263.3		247.0	
0.2	583.7		500.1		504.8		417.2		398.8		335.7		323.3		304.8		285.6	
0.25	658.6		563.4		576.2		484.5		461.3		396.8		376.8		356.1		334.7	
0.3	731.6		626.3		645.0		556.2		524.3		458.3		431.9		407.4		385.4	
0.35	798.8		688.8		712.5		631.2		588.1		519.7		489.4		459.1		439.1	
0.4	865.2		752.5		777.3		709.0		653.8		580.9		549.9		511.7		495.7	
0.45	923.9		817.3		841.7		786.2		720.0		642.7		611.8		566.6		557.7	
0.5	982.7		883.4		905.0		863.1		789.3		704.9		676.4		624.5		622.4	
0.55	1040.4		952.4		967.9		936.1		858.6		770.0		742.5		687.0		691.6	
0.6	1096.4		1021.4		1031.1		1009.1		931.3		836.0		811.5		754.9		764.0	
0.65	1152.3		1097.2		1096.4		1081.1		1004.1		908.2		882.3		828.8		838.7	
0.7	1208,3		1172.9		1161.6		1152.8		1081.4		983.8		957.6		909.3		916.8	
0.75	1272.8		1253.9		1228.2		1225.3		1159.8		1069.0		1035.0		994.6		996.3	
0.8	1339.5		1343.3		1306.9		1307.9		1242.2		1163.2		1122.4		1088.6		1083.8	
0.84	1393.0		1414.8		1369.8		1374.0		1318.5		1245.5		1192.4		1166.7		1156.5	
0.85	1406.3		1432.7		1385.5		1390.5		1337.5		1271.5		1209.8		1186.2		1174.7	
0.9	1485.0		1551.0		1467.2		1481.7		1432.8		1401.4		1327.7		1305.6		1286.4	
0.95	1612.5		1682.1		1604.2		1618.5		1576.7		1578.7		1449.6		1436.3		1418.9	
1	1740.0		2060.0		2060.0		2060.0		1740.0		2060.0		1740.0		1740.0		1740.0	
Sauter	739.69		654.73		615.53		553.54		492.43		420.79		414.76		398.97		358.34	

Table 4.1: Measurement results for various nozzle pressure conditions [Kittinger and Lubensky, 2014]

Chapter 5

Application of the DPM

The model developed in this work has been implemented to describe time-varying dispersion of lycopodium particles in a pipe and spreading of the chlorin and ammoniak in the environment. Additionally, it has been extended and adapted for Flash-Reactor pilot plant developed for recovery of zinc and iron from steel mill dusts.

5.1 Time-varying dispersion of Lycopodium particles in a pipe

The simulation model created in OpenFOAM® describes dispersion of lycopodium particles with uniform distribution ($d_p = 30\mu m$) of 10^5 injected representative parcels per second. Simulation results are used to develop experimental model for dust explosions, especially position for dust injection, mass flow and time needed to achieve, as far as possible, homogeneous dust concentration of $200g/cm^3$ in the entire volume. Euler-Lagrange approach was used for the air-filled pipe under ambient conditions with the surface area defined as wall boundary and four injection areas symmetrically positioned around the center origin of circular inlet surface.

Turbulent motion of continuous phase caused by spreading of free falling particles, especially in a near wall region, is modeled using modified low Reynolds k-epsilon model.

The number of collisions between particles is considered negligibly small and therefore only rebound interaction of the particles on the wall boundary is of relevance.

Stochastic discrete random walk model is implemented to predict particle dispersion under the influence of turbulent motion in the continuous phase.

Relaxation factors used in OpenFOAM case are given in Table 5.1

Table 5.2 summarizes set up for numerical schemes used in OpenFOAM for the solution of relevant equations.

Fields/Equations	**Under-Relaxation factor**
fields	
p	0.5
rho	0.9
equations	
U,k	0.5
epsilon	0.3

Table 5.1: Under-Relaxation factors OpenFOAM

Schemes	**Discretization**
ddtSchemes	Euler
gradSchemes	Gauss linear
divSchemes	
div(phi,U)	Gauss linearUpwindV
div(phid,p)	Gauss upwind
div(phi,k)	Gauss upwind
div(phi,h)	Gauss upwind
div(phi,epsilon)	Gauss upwind
div(U)	Gauss linear
div(muEff*dev2(T(grad(U))	Gauss linear
div(R)	Gauss linear
div(rho*R)	Gauss linear
div(phi*R)	Gauss upwind
laplacianSchemes	Gauss linear corrected
interpolationSchemes	linear
snGradSchemes	corrected

Table 5.2: Numerical schemes OpenFOAM

Particle velocity in m/s and mass concentration of lycopodium in kg/m^3 in the pipe over the time in a plane perpendicular to the inlet surface that includes axis of rotation is shown in Figure 5.1 to Figure 5.8.

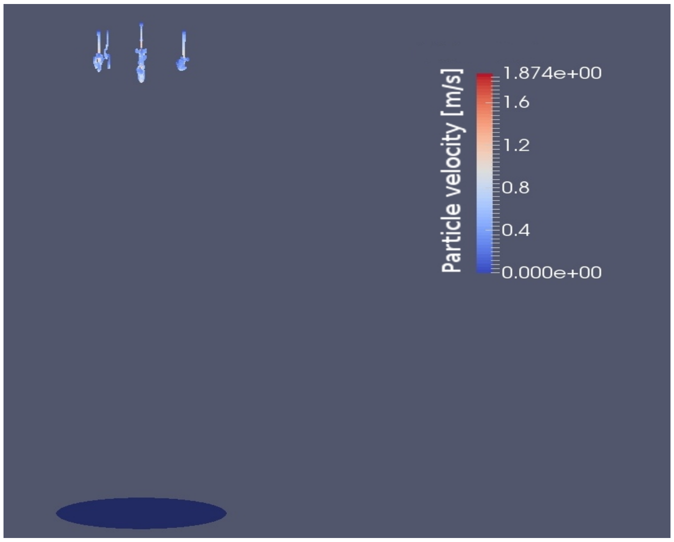

(a) Particle velocity profile

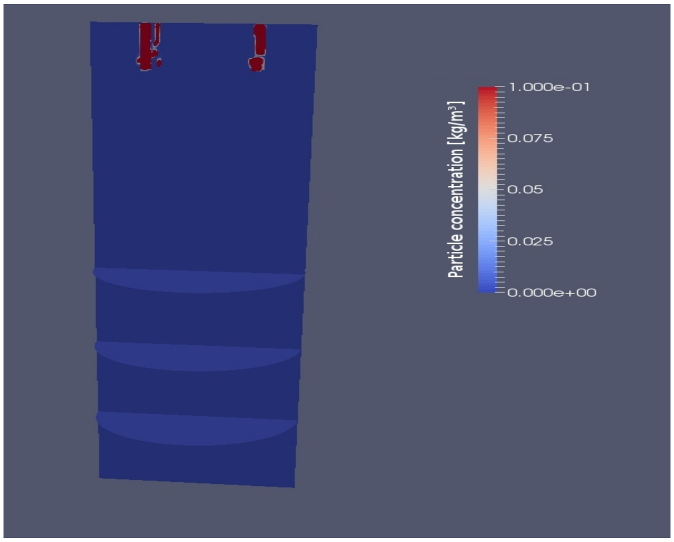

(b) Particle concentration

Figure 5.1: Particle velocity profile and concentration t=0.5s

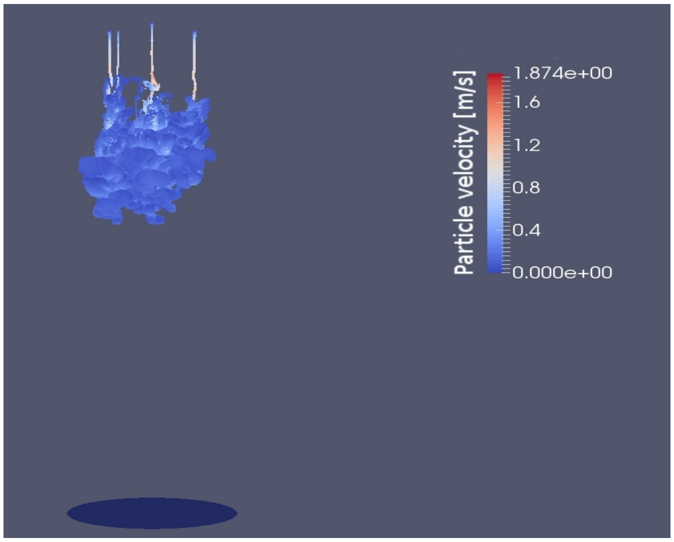

(a) Particle velocity profile

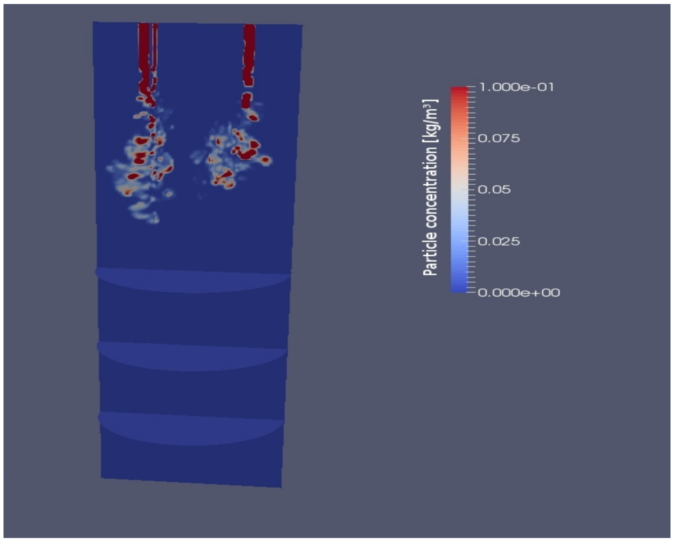

(b) Particle concentration

Figure 5.2: Particle velocity profile and concentration t=2.5s

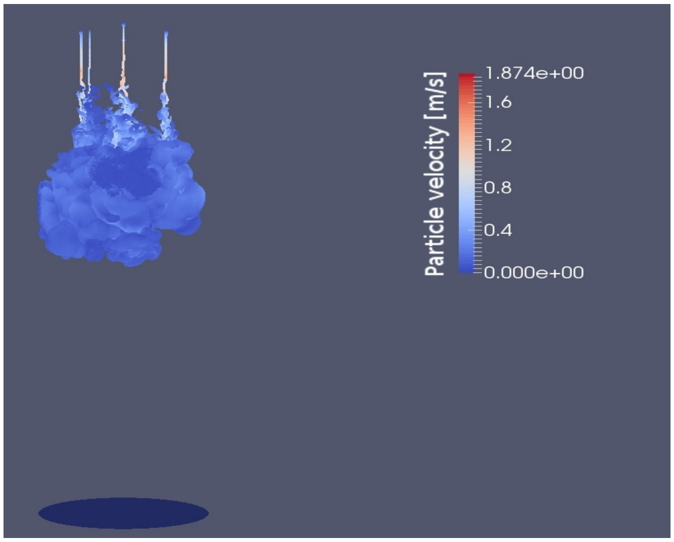

(a) Particle velocity profile

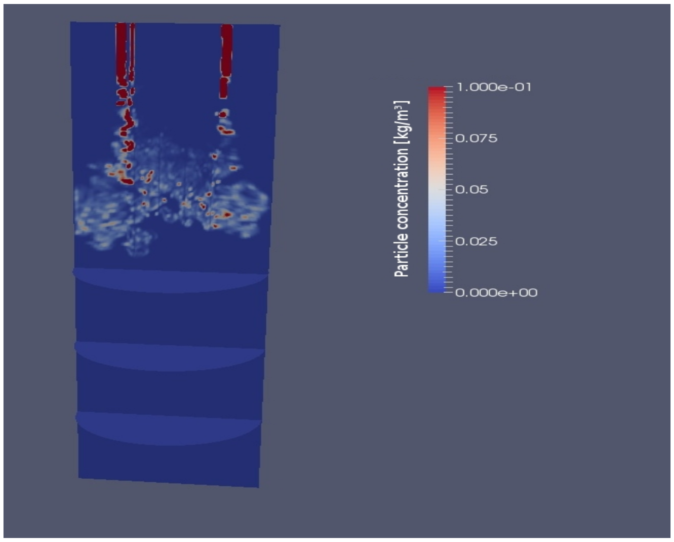

(b) Particle concentration

Figure 5.3: Particle velocity profile and concentration t=4.5s

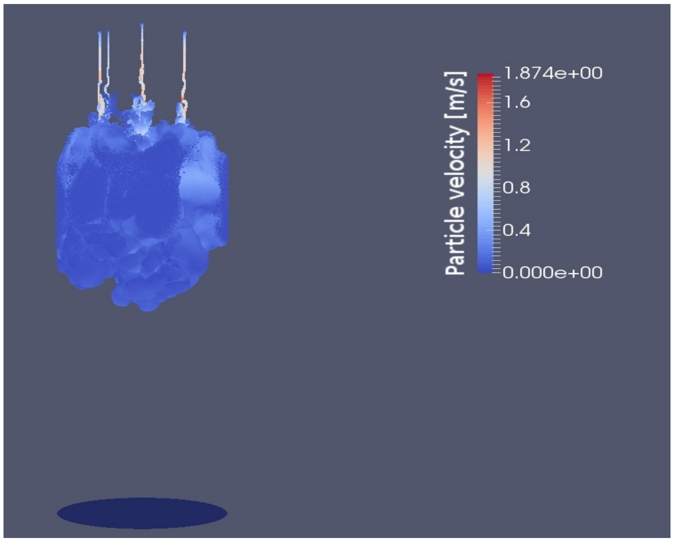

(a) Particle velocity profile

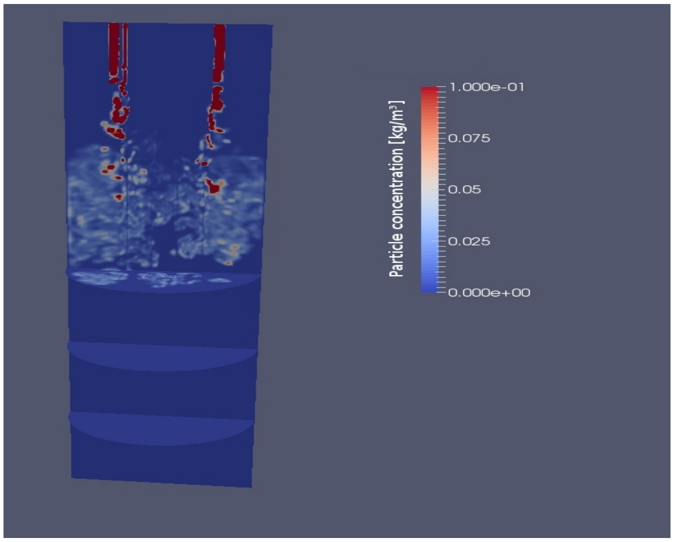

(b) Particle concentration

Figure 5.4: Particle velocity profile and concentration t=6.5s

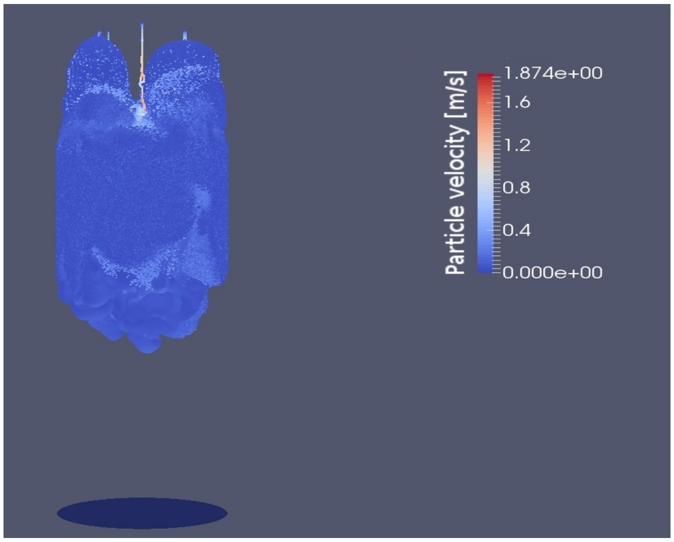

(a) Particle velocity profile

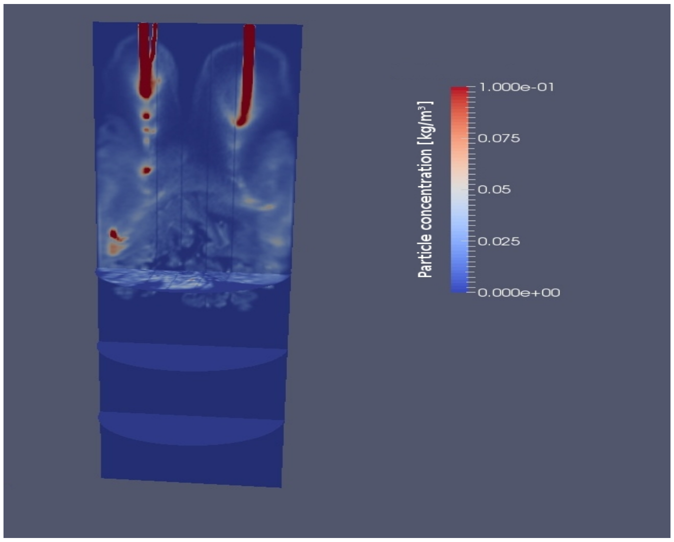

(b) Particle concentration

Figure 5.5: Particle velocity profile and concentration t=8.5s

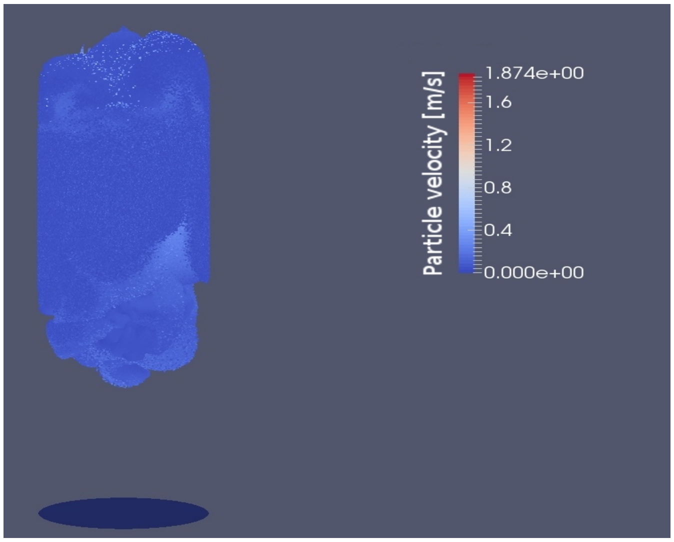

(a) Particle velocity profile

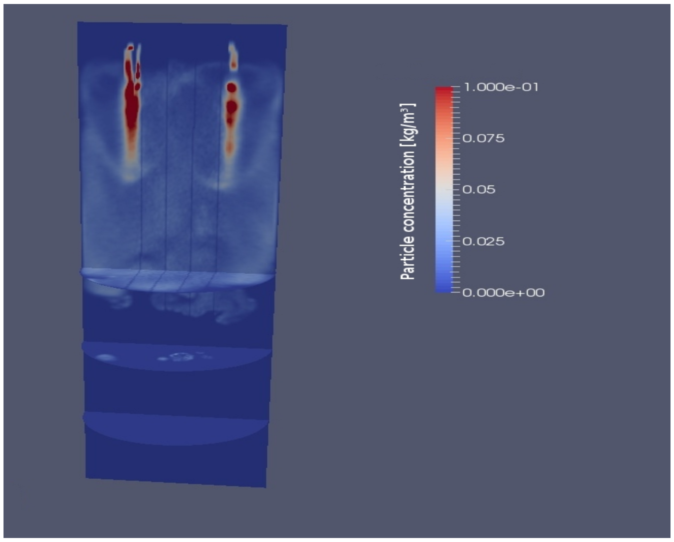

(b) Particle concentration

Figure 5.6: Particle velocity profile and concentration t=10.5s

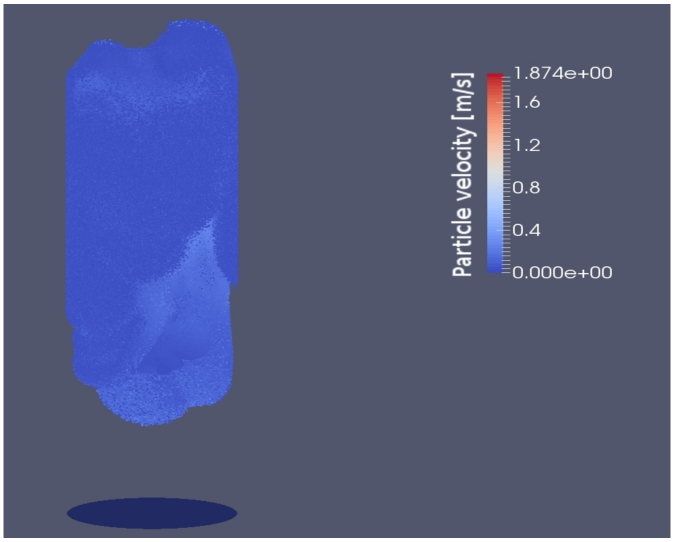

(a) Particle velocity profile

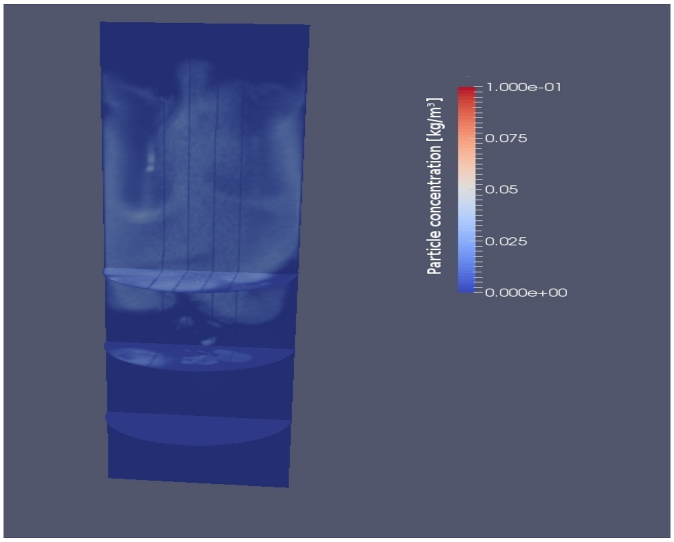

(b) Particle concentration

Figure 5.7: Particle velocity profile and concentration t=12.5s

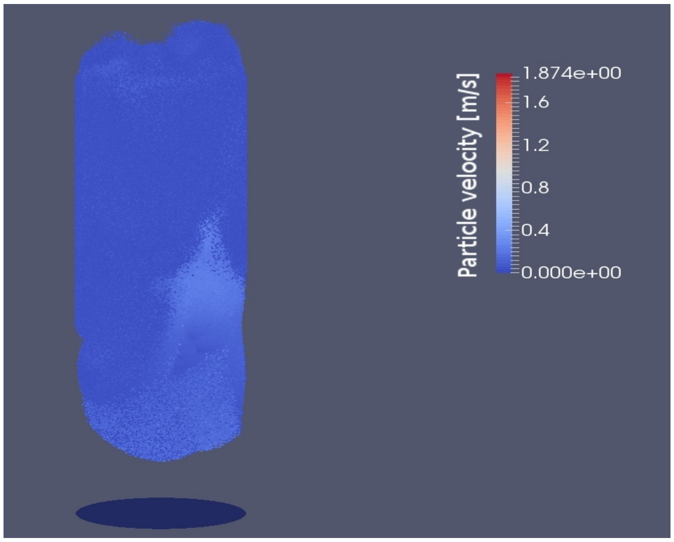

(a) Particle velocity profile

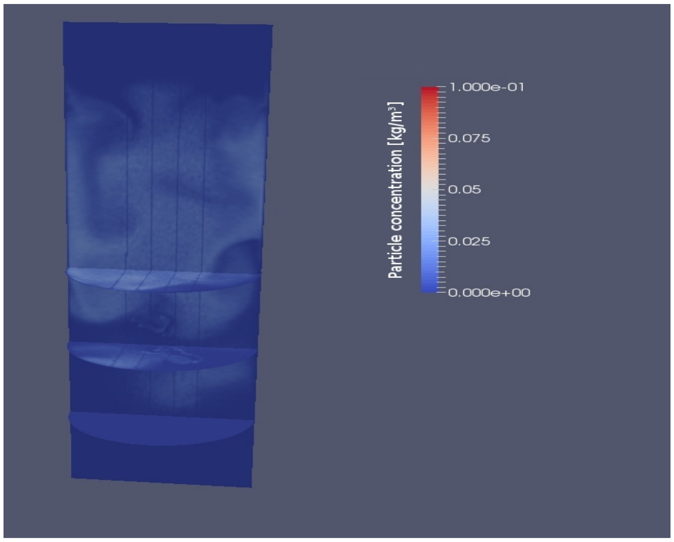

(b) Particle concentration

Figure 5.8: Particle velocity profile and concentration t=14.5s

5.2 Dispersion of Ammonia and Chlorin

In order to predict chlorin and ammoniak spreading in the environment with constant ambient conditions (air, 1 bar, 25°C), discretized geometry includes $1m^2$ area source of spreading toxic gas, two parallel rows of nozzles inclined at an angle of ±20° to the yz plane and constant wind velocity in x direction.

The trajectory of the dispersed drops are calculated as the Lagrangian phase, concentrations of the components in the surrounding air as Eulerian phase and additionally an user defined function in a C programming language for the absorption of the gases in the water drops has been implemented in ANSYS-FLUENT®. Additionally, a chemical kinetics to dechlorinate water drops with sodium thiosulfate has been implemented, but due to almost instantaneous reaction with chlorin very small particle time step size is needed to simulate interaction between phases, which leads to unaffordable high computational costs. For the description of turbulence phenomena, k-epsilon relizable model was used as the most suitable for turbulent axisymmetric free jet flow.

Statistical propagation of spray concentration under the influence of the turbulent eddies around the mean trajectory in the continuous phase is approximated using cloud model. Secondary brake up of droplets caused by deformation due to oscillation and distortion in the interaction with continuous phase is modelled using Taylor Analogy Breakup model. For the higher wind velocities in x direction, particle collision effect becomes significant, as can be seen in Figure 5.9, and has to be considered as well.

Table 5.3 summarizes discretization schemes used for the numerical solution of relevant equations. Calculations are started with using first order and after stabilization of the residuals switched to second order scheme.

Equation	**Discretization**
Pressure	Standard
Momentum	Second Order Upwind
Turbulent Kinetic Energy	Second Order Upwind
Turbulent Dissipation Rate	Second Order Upwind
Energy	Second Order Upwind
Species	Second Order Upwind

Table 5.3: Discretisation schemes

Under-relaxation factors given in Table 5.4 are used to achieve stability of the implemented numerical model. It should be noted that discrete phase relaxation factor is sequentially increased to the given value.

Equation	**Under-Relaxation factor**
Pressure	0.4
Density	0.8
Body Force	0.8
Momentum	0.6
Turbulent Kinetic Energy	0.5
Turbulent Dissipation Rate	0.5
Turbulent viscosity	0.7
Species	0.95
Energy	0.95
Discrete Phase Sources	0.5

Table 5.4: Underrelaxation factors

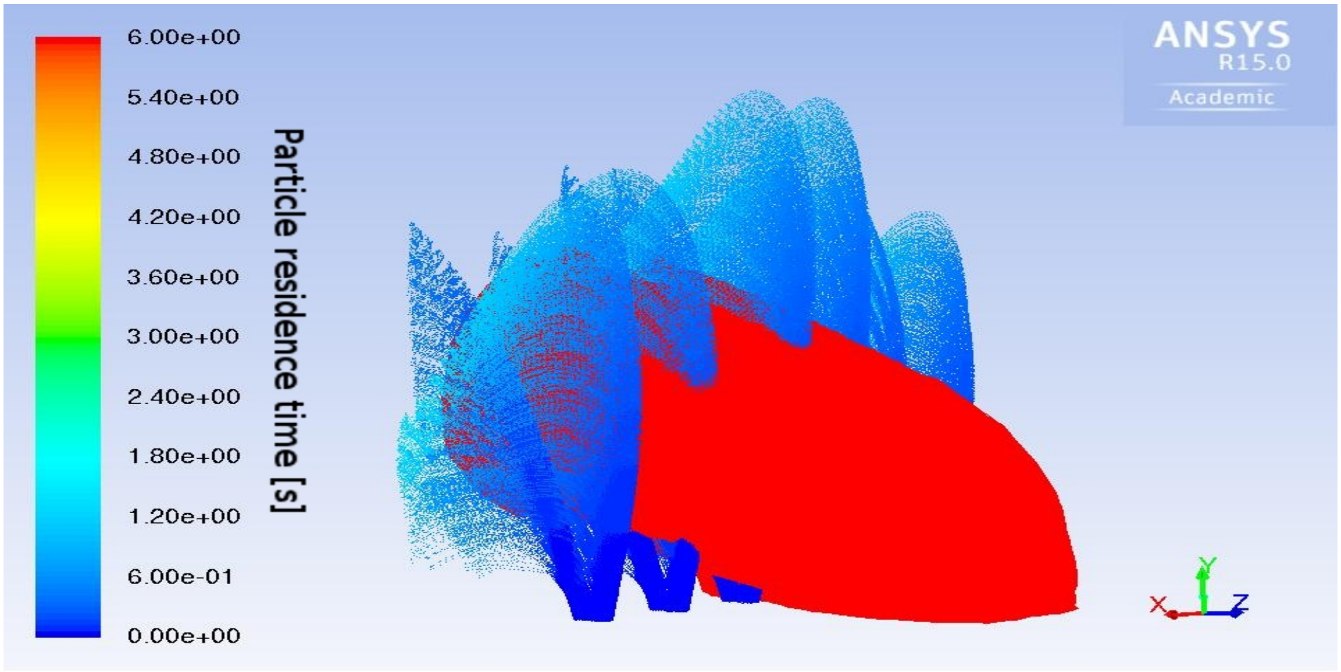

Figure 5.9: Isosurface for volume fraction $\nu_{NH_3} = 0.1$, wind velocity $U_x = 4m/s$, NH_3 total mass flow $\dot{m} = 5kg/s$

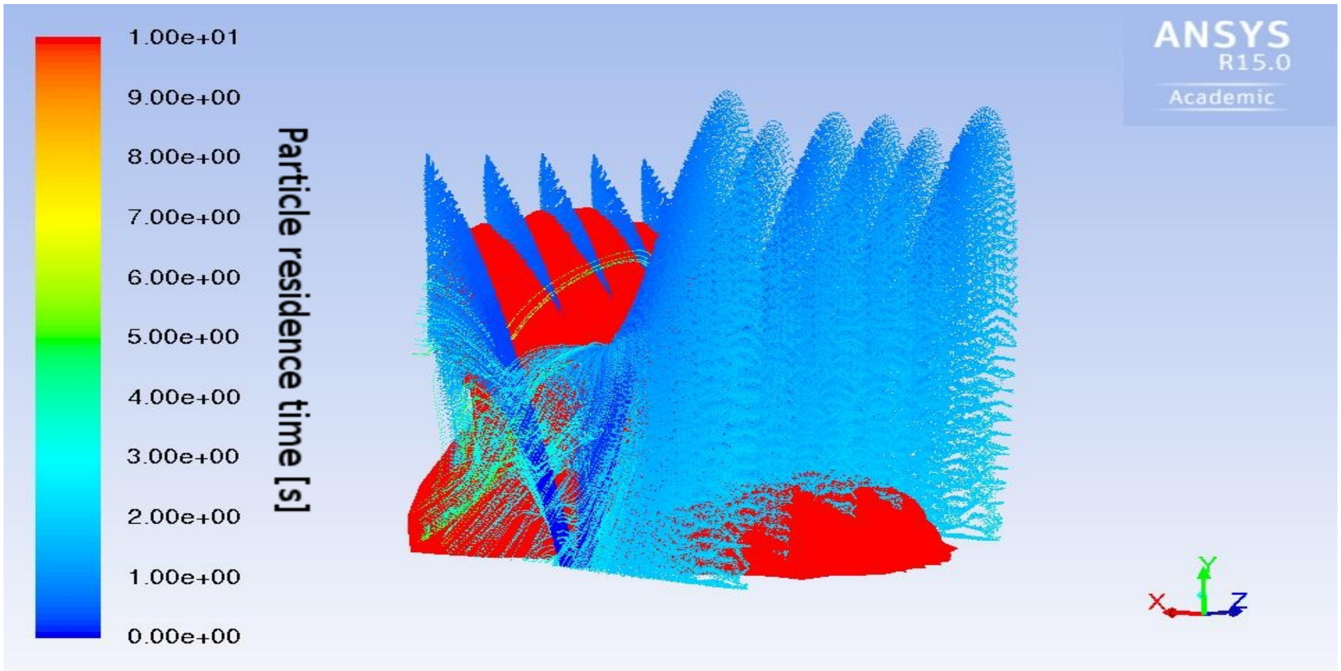

Figure 5.10: Isosurface Cl volume fraction $\nu_{Cl} = 0.01$, wind velocity $U_x = 1m/s$, Cl total mass flow $\dot{m} = 0.1kg/s$

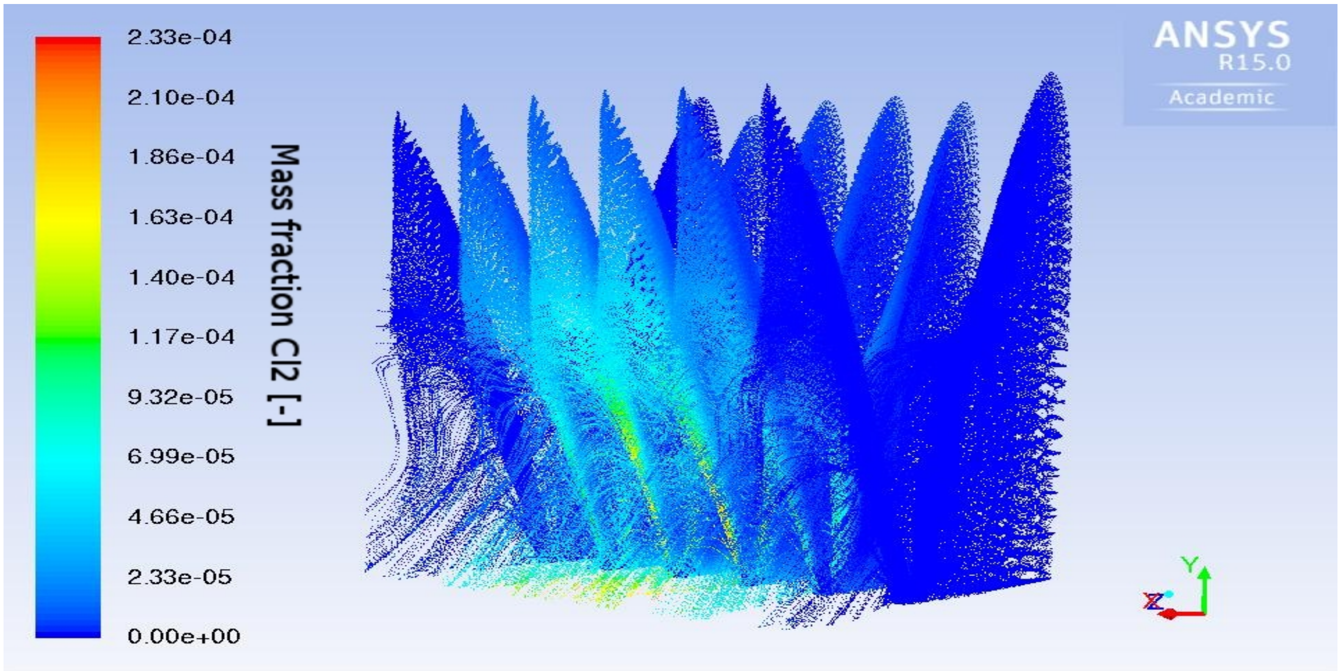

Figure 5.11: Mass transfer Cl , wind velocity $U_x = 1m/s$, Cl total mass flow $\dot{m} = 0.1kg/s$

List of Tables

List of Figures

Bibliography

S. K. Aggarwal and F. Peng. A review of droplet dynamics and vaporization modeling for engineering calculations. *Journal of Engineering for Gas Turbines and Power*, 117(3):453, 1995. ISSN 07424795. doi: 10.1115/1.2814117.

Ansys Inc. *ANSYS Fluent Theory Guide*. 2013.

A. G. Bailey, W. Balachandran, and T. J. Williams. The rosin—rammler size distribution for liquid droplet ensembles. *Journal of Aerosol Science*, 14(1):39–46, 1983. ISSN 00218502. doi: 10.1016/0021-8502(83)90083-6.

C. G. Ball, H. Fellouah, and A. Pollard. The flow field in turbulent round free jets. *Progress in Aerospace Sciences*, 50:1–26, 2012. ISSN 03760421. doi: 10.1016/j.paerosci.2011.10.002.

L. L. Baxter and P. J. Smith. Turbulent dispersion of particles: the stp model. *Energy & Fuels*, 7(6):852–859, 1993. ISSN 0887-0624. doi: 10.1021/ef00042a022.

Adrian Bejan and Allan D. Kraus. *Heat transfer handbook*. J. Wiley, New York, 2003. ISBN 0-471-39015-1.

Christo Boyadjiev. *Theoretical Chemical Engineering: Modeling and Simulation*. Springer Berlin, Berlin, aufl. 2010 edition, 2014. ISBN 978-3-642-43504-1.

Günter Brenn and Helfried Steiner. *Strömungslehre und wärmeübertragung II VT*. 2005.

Jinho Cha, Seungho Lim, Taejoon Kim, and Weon Gyu Shin. The effect of the reynolds number on the velocity and temperature distributions of a turbulent condensing jet. *International Journal of Heat and Fluid Flow*, 67:125–132, 2017. ISSN 0142727X. doi: 10.1016/j.ijheatfluidflow.2017.08.001.

Eberhart Chad, David M. Lineberry, and Marlow D. Moser. Experimental cold flow characterization of a swirl coaxial injector element. 2009.

Roland Clift, John Grace, and Martin E. Weber. *Bubbles, drops, and particles*. Dover, Mineola, dover ed edition, 2013. ISBN 978-0486445809.

P. A. Cundall and Strack, O. D. L. A discrete numerical model for granular assemblies. *Géotechnique*, 29(1):47–65, 1979. ISSN 0016-8505. doi: 10.1680/geot.1979.29.1.47.

Christophe Dumouchel. The maximum entropy formalism and the prediction of liquid spray drop-size distribution. *Entropy*, 11(4):713–747, 2009. ISSN 1099-4300. doi: 10.3390/e11040713.

Paul Eisenklam, S. A. Arunachalam, and J. A. Weston. Evaporation rates and drag resistance of burning drops. *Symposium (International) on Combustion*, 11(1):715–728, 1967. ISSN 00820784. doi: 10.1016/S0082-0784(67)80197-8.

Joel H. Ferziger and M. Perić. *Computational methods for fluid dynamics*. Springer, Berlin and New York, 3rd, rev. ed edition, 2002. ISBN 3-540-42074-6.

Smith Francis and Harvey Allan. Avoid common pitfails when using henry's law. 2007.

Edward N. Fuller, Paul D. Schettler, and J. Calvin. Giddings. New method for prediction of binary gas-phase diffusion coefficients. *Industrial & Engineering Chemistry*, 58(5):18–27, 1966. ISSN 0019-7866. doi: 10.1021/ie50677a007.

Guangyuan Sun. *Stochastic Simulation of Lagrangian Particle Transport in Turbulent Flows*. PhD thesis, Ira A. Fulton College of Engineering and Technology and Chemical Engineering, 2015.

Hussein J. Hussein, Steven P. Capp, and William K. George. Velocity measurements in a high-reynolds-number, momentum-conserving, axisymmetric, turbulent jet. *Journal of Fluid Mechanics*, 258(-1):31, 1994. ISSN 0022-1120. doi: 10.1017/S002211209400323X.

Runsten Josef. Droplet collisions in dieselspray and implementations of collisions in solidparticle. 2010.

Woo Tae Kim, Sushanta K. Mitra, Xianguo Li, L. A. Prociw, and Hu, T.C.J. A predictive model for the initial droplet size and velocity distributions in sprays and comparison with experiments. *Particle & Particle Systems Characterization*, 20(2):135–149, 2003. ISSN 09340866. doi: 10.1002/ppsc.200390011.

Fritz Kittinger and Jan Lubensky. Tropfengrößenanalyse: Interner laborbericht, lehrstuhl für verfahrenstechnik des industriellen umweltschutzes, montanuniversität leoben. 2014.

Manfred Klell. *Höhere Thermodynamik*. 2012.

R. Krishna and J. A. Wesselingh. The maxwell-stefan approach to mass transfer. *Chemical Engineering Science*, 52(6):861–911, 1997. ISSN 00092509. doi: 10.1016/S0009-2509(96)00458-7.

B. E. Launder, G. J. Reece, and W. Rodi. Progress in the development of a reynolds-stress turbulence closure. *Journal of Fluid Mechanics*, 68(03):537, 1975. ISSN 0022-1120. doi: 10.1017/S0022112075001814.

Min Wook Lee, Jung Jae Park, Massoud Massoudi Farid, and Sam S. Yoon. Comparison and correction of the drop breakup models for stochastic dilute spray flow. *Applied Mathematical Modelling*, 36(9):4512–4520, 2012. ISSN 0307904X. doi: 10.1016/j.apm.2012.02.015.

Arthur H. Lefebvre and Vincent G. McDonell. *Atomization and sprays*. CRC Press, Taylor & Francis Group, Boca Raton and London and New York, second edition edition, 2017. ISBN 978-1-4987-3625-1.

W. K. Lewis and W. G. Whitman. Principles of gas absorption. *Industrial & Engineering Chemistry*, 16(12): 1215–1220, 1924. ISSN 0019-7866. doi: 10.1021/ie50180a002.

F. R. Menter. Two-equation eddy-viscosity turbulence models for engineering applications. *AIAA Journal*, 32(8):1598–1605, 1994. ISSN 0001-1452. doi: 10.2514/3.12149.

Efstathios Michaelides. *Particles, Bubbles & Drops.* 2006. ISBN 981-256-647-3.

Ali Mohammad-Djafari. A matlab program to calculate the maximum entropy distributions. 2002.

S. A. Morsi and A. J. Alexander. An investigation of particle trajectories in two-phase flow systems. *Journal of Fluid Mechanics*, 55(02):193, 1972. ISSN 0022-1120. doi: 10.1017/S0022112072001806.

F. Moukalled, L. Mangani, and M. Darwish. *The Finite Volume Method in Computational Fluid Dynamics: An Advanced Introduction with OpenFOAM® and Matlab*, volume 113 of *Fluid Mechanics and Its Applications.* Springer International Publishing, Cham, 1st ed. 2015 edition, 2016. ISBN 978-3-319-16874-6.

E. Movahednejad, F. Ommi, S. M. Hosseinalipour, C. P. Chen, and S. A. Mahdavi. Application of maximum entropy method for droplet size distribution prediction using instability analysis of liquid sheet. *Heat and Mass Transfer*, 47(12):1591–1600, 2011. ISSN 0947-7411. doi: 10.1007/s00231-011-0797-5.

Ehsan Movahednejad, Fathollah Ommi, and S. Mostafa Hosseinalipour. Prediction of droplet size and velocity distribution in droplet formation region of liquid spray. *Entropy*, 12(6):1484–1498, 2010. ISSN 1099-4300. doi: 10.3390/e12061484.

Peter J. O'Rourke and Anthony A. Amsden. The tab method for numerical calculation of spray droplet breakup. In *1987 SAE International Fall Fuels and Lubricants Meeting and Exhibition*, SAE Technical Paper Series. SAE International400 Commonwealth Drive, Warrendale, PA, United States, 1987. doi: 10.4271/872089.

Peter J. O'Rourke, Anthony A. Amsden, and T. D. Butler. *KIVA-II: A Computer Program for Chemically Reactive Flows with Sprays.* 1989.

G. D. Raithby and E. H. Chui. A finite-volume method for predicting a radiant heat transfer in enclosures with participating media. *Journal of Heat Transfer*, 112(2):415, 1990. ISSN 00221481. doi: 10.1115/1.2910394.

M. C. Roco. *Particulate two-phase flow.* Butterworth-Heinemann series in chemical engineering. Butterworth-Heinemann, Boston, 1993. ISBN 0750692758.

J.-R Sack and J. Urrutia. *Handbook of computational geometry.* Elsevier, Amsterdam [etc.], 2008. ISBN 978-0-444-82537-7.

Tsan-Hsing Shih, William W. Liou, Aamir Shabbir, Zhigang Yang, and Jiang Zhu. A new k- eddy viscosity model for high reynolds number turbulent flows. *Computers & Fluids*, 24(3):227–238, 1995. ISSN 00457930. doi: 10.1016/0045-7930(94)00032-T.

Boris Springborn. *A Variational Principle for Weighted Delaunay Triangulations and Hyperideal Polyhedra*. 2008.

Stephen Kern Robertson. *The Kinematics of Turbulent Boundary Layer Structure*. 1991.

L. Talbot, R. K. Cheng, R. W. Schefer, and D. R. Willis. Thermophoresis of particles in a heated boundary layer. *Journal of Fluid Mechanics*, 101(04):737, 1980. ISSN 0022-1120. doi: 10.1017/S0022112080001905.

Prakash D. Vaidya and Eugeny Y. Kenig. Gas–liquid reaction kinetics: A review of determination methods. *Chemical Engineering Communications*, 194(12):1543–1565, 2007. ISSN 0098-6445. doi: 10.1080/00986440701518314.

David C. Wilcox. *Turbulence modeling for CFD.* DCW Industries, La Cañada and Calif, 3. ed., 2. print edition, 2010. ISBN 1928729088.

M. C. YUEN and L. W. CHEN. On drag of evaporating liquid droplets. *Combustion Science and Technology*, 14(4-6):147–154, 1976. ISSN 0010-2202. doi: 10.1080/00102207608547524.